ZTF Early Observations of Type Ia Supernovae II:
First Light, the Initial Rise, and Time to Reach Maximum Brightness

A. A. Miller,[1,2] Y. Yao,[3] M. Bulla,[4] C. Pankow,[1] E. C. Bellm,[5] S. B. Cenko,[6,7] R. Dekany,[8] C. Fremling,[3] M. J. Graham,[9]
T. Kupfer,[10] R. R. Laher,[11] A. A. Mahabal,[9,12] F. J. Masci,[11] P. E. Nugent,[13,14] R. Riddle,[8] B. Rusholme,[11] R. M. Smith,[8]
D. L. Shupe,[11] J. van Roestel,[9] and S. R. Kulkarni[3]

[1]*Center for Interdisciplinary Exploration and Research in Astrophysics (CIERA) and Department of Physics and Astronomy, Northwestern University, 2145 Sheridan Road, Evanston, IL 60208, USA*

[2]*The Adler Planetarium, Chicago, IL 60605, USA*

[3]*Cahill Center for Astrophysics, California Institute of Technology, 1200 E. California Boulevard, Pasadena, CA 91125, USA*

[4]*Nordita, KTH Royal Institute of Technology and Stockholm University, Roslagstullsbacken 23, SE-106 91 Stockholm, Sweden*

[5]*DIRAC Institute, Department of Astronomy, University of Washington, 3910 15th Avenue NE, Seattle, WA 98195, USA*

[6]*Astrophysics Science Division, NASA Goddard Space Flight Center, 8800 Greenbelt Road, Greenbelt, MD 20771, USA*

[7]*Joint Space-Science Institute, University of Maryland, College Park, MD 20742, USA*

[8]*Caltech Optical Observatories, California Institute of Technology, Pasadena, CA 91125, USA*

[9]*Division of Physics, Mathematics, and Astronomy, California Institute of Technology, Pasadena, CA 91125, USA*

[10]*Kavli Institute for Theoretical Physics, University of California, Santa Barbara, CA 93106, USA*

[11]*IPAC, California Institute of Technology, 1200 E. California Blvd, Pasadena, CA 91125, USA*

[12]*Center for Data Driven Discovery, California Institute of Technology, Pasadena, CA 91125, USA*

[13]*Computational Cosmology Center, Lawrence Berkeley National Laboratory, 1 Cyclotron Road, Berkeley, CA 94720, USA*

[14]*Department of Astronomy, University of California, Berkeley, CA 94720-3411, USA*

Abstract

While it is clear that Type Ia supernovae (SNe) are the result of thermonuclear explosions in C/O white dwarfs (WDs), a great deal remains uncertain about the binary companion that facilitates the explosive disruption of the WD. Here, we present a comprehensive analysis of a unique, and large, data set of 127 SNe Ia with exquisite coverage by the Zwicky Transient Facility (ZTF). High-cadence (6 observations per night) ZTF observations allow us to measure the SN rise time and examine its initial evolution. We develop a Bayesian framework to model the early rise as a power-law in time, which enables the inclusion of priors in our model. For a volume-limited subset of normal SNe Ia, we find the mean power-law index is consistent with 2 in the r_{ZTF}-band ($\alpha_r = 2.01 \pm 0.02$), as expected in the expanding fireball model. There are, however, individual SNe that are clearly inconsistent with $\alpha_r = 2$. We estimate a mean rise time of 18.5 d (with a range extending from $\sim$15–22 d), though this is subject to the adopted prior. We identify an important, previously unknown, bias whereby the rise times for higher redshift SNe within a flux-limited survey are systematically underestimated. This effect can be partially alleviated if the power-law index is fixed to $\alpha = 2$, in which case we estimate a mean rise time of 21.0 d (with a range from $\sim$18–23 d). The sample includes a handful or rare and peculiar SNe Ia. Finally, we conclude with a discussion of lessons learned from the ZTF sample that can eventually be applied to Large Synoptic Survey Telescope observations.

amiller@northwestern.edu

arXiv:2001.00598v2 [astro-ph.HE] 7 Jan 2020

1. Introduction

The fact that supernovae (SNe) of Type Ia can be empirically calibrated as standardizable candles makes them arguably the most important tool in all of physics for the past ∼two decades. By unlocking our ability to accurately measure distances at high redshift, SNe Ia have completely revolutionized our understanding of the Universe (Riess et al. 1998; Perlmutter et al. 1999). While it is all but certain that SNe Ia are the result of thermonuclear explosions in carbon-oxygen (C/O) white dwarfs (WDs) in binary star systems (see Maoz et al. 2014; Livio & Mazzali 2018 for recent reviews), there remains a great deal about SNe Ia progenitors and the precise explosion mechanism that we do not know. This leads to the tantalizing hope that an improved understanding of the binary companions or explosion may improve our ability to calibrate these explosions as standardizable candles.

One clear avenue for better understanding the progenitors of SNe Ia is to obtain observations in the hours to days after explosion (Maoz et al. 2014). Such detections provide an opportunity to probe the progenitor environment and binary companion, which is simply not possible once the SN evolves well into the expansion phase (they are standardizable precisely because they are all nearly identical at maximum light). Indeed, in the landmark discovery of SN 2011fe by the Palomar Transient Factory (PTF; Law et al. 2009; Rau et al. 2009), Nugent et al. (2011) were able to constrain the time of explosion to ±20 min (though see Piro & Nakar 2013 for an explanation of a potential early "dark phase"). Bloom et al. (2012) would later combine the PTF observations with an early non-detection while comparing the limits to shock-breakout models to constrain the size of the progenitor to be $\lesssim 0.01 R_\odot$, providing the most direct evidence to date that SNe Ia come from WDs. These critical findings have demonstrated the importance of high-cadence time-domain surveys for discovering SNe shortly after explosion.

Pinning down the binary companion to the exploding WD remains a challenge. There are likely two dominant pathways towards explosion. In the first, the WD accretes H from a non-degenerate companion and eventually explodes as it approaches the Chandrasekhar mass ($M_{\rm Ch}$; known as the single degenerate, or SD, scenario; Whelan & Iben 1973), while in the second the explosion follows the interaction or merger of two WD stars (known as the double degenerate, or DD, scenario; Web-bink 1984). While the debate long focused on which of these two scenarios is correct, there is now strong empirical evidence in support of both channels. PTF 11kx, an extreme example of a SN Ia, showed clear evidence of multiple shells of circumstellar material (Dilday et al. 2012), which is precisely what one would expect in a WD+red giant system that had undergone multiple novae prior to the final, fatal thermonuclear explosion. On the other hand, hypervelocity WDs discovered by *Gaia* are likely the surviving companions of DD explosions (Shen et al. 2018).

There is also emerging evidence that WDs can explode prior to reaching $M_{\rm Ch}$. Detailed modeling of SNe Ia light curves (Scalzo et al. 2014) and a blue-to-red-to-blue color evolution observed in a few SNe (Jiang et al. 2017; Noebauer et al. 2017; Polin et al. 2019; De et al. 2019), point to sub-$M_{\rm Ch}$ mass explosions. Such explosions are possible if a C/O WD accretes and retains a thick He shell. A detonation in this shell can trigger an explosion in the C/O core of the WD (e.g., Nomoto 1982a,b).

Now the most pressing questions are the following: which scenario, SD or DD, and which mass explosion, $M_{\rm Ch}$ or sub-$M_{\rm Ch}$, is dominant?

Here too, early observations should prove useful. In the SD scenario the SN ejecta will collide with the non-degenerate companion creating a shock that gives rise to a bright ultraviolet/optical flash in the days after explosion (Kasen 2010). To date, the search for such a signature in large samples typically results in a non-detection (e.g., Hayden et al. 2010; Ganeshalingam et al. 2011; Bianco et al. 2011).[1] For the DD scenario, some sub-$M_{\rm Ch}$ DD explosions exhibit a highly unusual color evolution, though this can only be observed a few days after explosion (Noebauer et al. 2017; Polin et al. 2019).

Measurements of the rise time, i.e., the time it takes the SN to evolve from first light, the moment when optical photons diffuse out of the photosphere, to maximum brightness, can also play a role in constraining the progenitor systems of SNe Ia. Initial work to esti-

---

[1] There are claims of companion interaction based on short-lived optical "bumps" in the early light curves for individual SNe (e.g., Cao et al. 2015; Marion et al. 2016; Hosseinzadeh et al. 2017; Dimitriadis et al. 2019). Alternative models (e.g., Dessart et al. 2014; Piro & Morozova 2016) utilizing different physical scenarios can produce similar bumps, leading many (e.g., Kromer et al. 2016; Shappee et al. 2016a; Noebauer et al. 2017; Miller et al. 2018; Shappee et al. 2019) to appeal to alternative explanations than ejecta-companion interaction.

mate the rise times of SNe Ia clearly demonstrated that early efforts to model WD explosions significantly underestimated the opacities in the SN ejecta (e.g., Riess et al. 1999). Furthermore, while the famous luminosity-decline relationship for SNe Ia makes them standardizable (Phillips 1993), recent evidence suggests that the rise, rather than the decline, of SNe Ia is a better indicator of their peak luminosity (Hayden et al. 2019). Rise time measurements are most precise when a SN is discovered shortly after explosion, which only becomes routine with high-cadence observations.

In their seminal study, Riess et al. (1999) found that the mean rise time of SNe Ia is 19.5 ± 0.2 d, *after correcting the individual SNe for their luminosity-decline relation* (we hereafter refer to these corrections as shape corrections). Aldering et al. (2000) would later point out that rise time estimates can be significantly biased if uncertainties in the time of maximum light are ignored. It was also found that the rise times of low- and high-redshift SNe are consistent (Aldering et al. 2000; Conley et al. 2006). In Hayden et al. (2010) and Ganeshalingam et al. (2011), similar approaches were applied to significantly larger samples of SNe, and shorter shape-corrected mean rise times were found.

As observational cadences have increased over the past ∼decade, there has been a surge of SNe Ia discovered shortly after explosion. This has led more recent efforts to focus on measuring the rise times of populations of individual SNe (e.g., Firth et al. 2015; Zheng et al. 2017; Papadogiannakis et al. 2019), which is the approach adopted in this study. The utility of avoiding shape corrections is that it allows one to search for multiple populations in the distribution of rise times, which could point to a multitude of explosion scenarios. While Papadogiannakis et al. (2019) find no evidence for multiple populations, Ganeshalingam et al. (2010) find that high-velocity SNe Ia rise ∼1.5 d faster than their normal counterparts.

We are now in an era where hydrodynamic radiation transport models have become very sophisticated. Accurate measurements of the observed distribution of SN Ia rise times can be compared with these models to rule out theoretical scenarios that evolve too quickly or too slowly (e.g., Magee et al. 2018). In a similar sense, every model produces unique predictions for the initial evolution of the SN (e.g., Dessart et al. 2014; Noebauer et al. 2017; Polin et al. 2019; Magee et al. 2019). Similarly, if the early emission is modeled as a power-law in time (i.e., $f \propto t^{\alpha}$), measures of the power-law index α can confirm, or reject, different explosion scenarios.

In this paper, the second in a series of three examining the photometric evolution of 127 SNe Ia with early ob-servations discovered by the Zwicky Transient Facility (ZTF; Bellm et al. 2019a; Graham et al. 2019) in 2018, we examine the rise time of SNe Ia and whether or not their early emission can be characterized as a simple power law. Paper I (Yao et al. 2019) describes the sample, while Paper III (M. Bulla et al. 2020, submitted) discusses the evolution of SNe Ia colors shortly after explosion. The sample, which is large, is equally impressive in its quality: ZTF observations are obtained in both the g_{ZTF} and r_{ZTF} filters every night. The nightly cadence critically allows us to include sub-threshold detections in our analysis of SNe Ia (Yao et al. 2019). This aspect of the ZTF sample separates it from other low-z data sets. We construct a Bayesian framework to estimate the rise time of individual SNe. An advantage of this approach, relative to other studies, is that it allows us to naturally incorporate priors into the model fitting. We uncover a systematic bias whereby the rise times of the higher redshift SNe within a flux-limited survey are typically underestimated. We show that the adoption of strong priors can, at least partially, alleviate this bias. Finally, we conclude with a discussion of lessons from ZTF that can be applied to the Large Synoptic Survey Telescope (LSST).

2. ZTF Photometry

The sample of 127 SNe Ia utilized in this study was defined in Yao et al. (2019), for the full details on our sample selection we refer the reader there. Briefly, the SNe studied herein were discovered in observations taken for the high-cadence extragalactic experiment conducted by the ZTF partnership in 2018 (Bellm et al. 2019b). This experiment monitors ∼3000 deg² on a nightly basis (over the 9 month period when the fields are visible), with the aim of obtaining 3 g_{ZTF} and 3 r_{ZTF} observations every night. In total, there were 247 spectroscopically confirmed SNe Ia discovered within these fields. The GROWTH Marshal (Kasliwal et al. 2019) is used to organize and visualize the data. Following cuts to limit the sample to SNe that were discovered "early" (defined as 10 d or more, in the SN rest frame, prior to the time of maximum light in the B-band, $t_{B,\mathrm{max}}$) and have high quality light curves, the sample was reduced to 127 SNe (see Yao et al. 2019 for the full details).

In Yao et al. (2019), we produced "forced" point-spread-function (PSF) photometry for each of the 127 SNe on every image where the SN was observed. The PSF model was generated as part of the ZTF real-time image subtraction pipeline (Masci et al. 2019), which uses an image-differencing technique based on Zackay et al. (2016). The forced PSF photometry procedure fixes the position of each SN and measures the PSF

flux in all images that contain the SN position, even in epochs where the signal-to-noise ratio (SNR) $\lesssim 1$ and the SN is not detected.

We normalize the SN flux relative to the observed peak flux in the $g_{\rm ZTF}$- and $r_{\rm ZTF}$-bands as measured by SALT2 (Guy et al. 2007; see Yao et al. 2019 for our SALT2 implementation details). The relative fluxes produced via this procedure are unique for every ZTF reference image (hereafter fcqf ID following the nomenclature in Yao et al. 2019). The ZTF field grid includes some overlap, and SNe that occur in overlap regions will have multiple fcqf IDs for a single filter. Estimates of the baseline flux must account for the individual fcqf IDs. In Yao et al. (2019), this baseline flux, C, and χ_ν^2, which accounts for underestimated uncertainties in the flux measurements, are used to correct the results of the forced PSF photometry. For this study, we ignore the corrections suggested in Yao et al. (2019) and instead incorporate these values into our model so they can be marginalized over and effectively ignored.

3. Modeling the Early Rise of SNe Ia

Following arguments first laid out in Riess et al. (1999), the rest-frame optical flux of a SN Ia should evolve $\propto t^2$ shortly after explosion. For an ideal, expanding fireball, the observed flux through a passband covering the Rayleigh-Jeans tail of the approximately blackbody emission will be $f \propto R^2 T = v^2 t^2 T$, where f is the SN flux, T is the blackbody temperature, R is photospheric radius, v is the ejecta velocity, and t is the time since explosion.[2] While these idealized conditions are not perfectly met in nature, T and v clearly change shortly after explosion (e.g., Parrent et al. 2012), their relative change is small compared to t. Thus, the "t^2-law" should approximately hold, and indeed many studies of large samples of SNe Ia have shown that in the blue optical filters $f \propto t^2$ to within the uncertainties (e.g., Conley et al. 2006; Hayden et al. 2010; Ganeshalingam et al. 2011). At the same time, several recent studies of individual, low-redshift SNe Ia show strong evidence that a power-law model for the SN flux only reproduces the data if the power-law index, α, is significantly lower than 2 (e.g., Zheng et al. 2013, 2014; Shappee et al. 2016b; Miller et al. 2018; Fausnaugh et al. 2019; Dimitriadis et al. 2019).

For this study, we characterize the early emission in a single filter from a SN Ia as a power law:

$$f_b(t) = C + H[t_{\rm fl}]A_b(t - t_{\rm fl})^{\alpha_b}, \qquad (1)$$

where $f_b(t)$ is the flux in filter b as a function of time t in the SN rest frame, C is a constant representing the baseline flux present in the reference image prior to the SN, $t_{\rm fl}$ is the time of first light,[3] $H[t_{\rm fl}]$ is the Heaviside function equal to 0 for $t < t_{\rm fl}$ and 1 for $t \geq t_{\rm fl}$, A_b is a constant of proportionality in filter b, and α_b is the power-law index describing the rise in filter b.

For ZTF, observations are obtained in the $g_{\rm ZTF}$- and $r_{\rm ZTF}$-bands, and, we model the evolution in both filters simultaneously. While, strictly speaking, $t_{{\rm fl},g} \neq t_{{\rm fl},r}$, we expect these values to be nearly identical given the similarity of the SN ejecta opacity at these wavelengths (e.g., Figure 6 in Magee et al. 2018), and assume we cannot resolve the difference with ZTF data. Therefore we adopt $t_{\rm fl}$ ($\approx t_{{\rm fl},g} \approx t_{{\rm fl},r}$) as a single parameter for our analysis. As discussed in Yao et al. (2019), C is a function of fcqf ID, which represents both the filter and ZTF field ID (see also §2).

Many of the SNe in our sample are observed at an extremely early phase in their evolution, at times when the spectral diversity in SNe Ia is not well constrained (see for example the bottom panel of Figure 1 in Guy et al. 2007). As a result, we do not apply K-corrections to the ZTF light curves prior to model fitting. Furthermore, without precise knowledge of the time of explosion, it is impossible to know which observations in the ZTF nightly sequence should be corrected and which should not. While examining SN 2011fe, Firth et al. (2015) find that ignoring K-corrections leads to a systematic uncertainty on α of ± 0.1, which is smaller than the typical uncertainty we measure (see §4). This suggests that our inability to apply K-corrections does not significantly affect our final conclusions.

If we assume the observed deviations between the model flux and the data are the result of Gaussian scatter, the log-likelihood for the data is:

$$\ln \mathscr{L} \propto -\frac{1}{2}\sum_{d,i}\frac{[f_{d,i} - f_d(t_i)]^2}{(\beta_d \sigma_{d,i})^2} - \sum \ln(\beta_d \sigma_{d,i}), \quad (2)$$

where the sum is over all fcqf IDs d and all observations i. $f_{d,i}$ is the $i^{\rm th}$ flux measurement with corresponding uncertainty $\sigma_{d,i}$, and β_d is a term we add to account for the fact that the uncertainties are underestimated (see Yao et al. 2019). Finally, $f_d(t_i)$ is the model, Equation 1 evaluated at the time of each observation t_i, with C replaced by C_d, the baseline for the individual fcqf IDs, and A_b and α_b replaced by $A_{b|d}$ and $\alpha_{b|d}$, respectively,

---

[2] All times reported in this study have been corrected to the SN rest frame.

[3] $t_{\rm fl}$ is not the time of explosion, but rather the time when optical emission begins for the SN, as the observed emission due to radioactive decay in the interior of the SN ejecta must first diffuse through the photosphere, see e.g., Piro & Nakar (2013, 2014).

as these terms depend on fcqf ID, but only the filter b and not the field ID.

Ultimately, we only care about 3 model parameters: $t_{\rm fl}$, and the power-law index describing the rise in the $g_{\rm ZTF}$ and $r_{\rm ZTF}$ filters, hereafter α_g and α_r, respectively. Following Bayes' Law, we multiply the likelihood by a prior and use an affine-invariant, ensemble Markov chain Monte Carlo (MCMC) technique (Goodman & Weare 2010) to approximate the model posterior.

There is a strong degeneracy between $A_{b|d}$ and $\alpha_{b|d}$, which we find can be removed with the following change of variables $A'_{b|d} = A_{b|d} 10^{\alpha_{b|d}}$ in Equation 1. We adopt Jeffreys prior (Jeffreys 1946) for the scale parameters $A_{b|d}$ and β_d, and wide flat priors for all other model parameters, as summarized in Table 1. The MCMC integration is performed using `emcee` (Foreman-Mackey et al. 2013). Within the ensemble, we use 100 walkers, each of which is run until convergence or 3 million steps, whichever comes first. We test for convergence by examining the average autocorrelation length of the individual chains τ after every 20,000 steps, and consider the chains converged if $n_{\rm steps} > 100\,\tau$, where $n_{\rm steps}$ is the total number of steps in each chain, and the change in τ relative to the previous estimate has changed by $< 1\%$.

Table 1. Model Parameters θ and Their Priors

θ	Description	Prior
C_d	baseline flux per fcqf ID d	$\mathcal{U}(-10^8, 10^8)$
$t_{\rm fl}$	time of first light	$\mathcal{U}(-100, 0)$
$A'_{b|d}$	proportionality factor per filter b	$A'_{b|d}{}^{-1} 10^{-\alpha_{b|d}}$
$\alpha_{b|d}$	rising power-law index per filter b	$\mathcal{U}(0, 10^8)$
β_d	uncertainty scale factor per fcqf ID d	β_d^{-1}

NOTE—The factor of $10^{-\alpha_{b|d}}$ in the prior for $A'_{b|d}$ follows from the change of variables (see Appendix A).

A key decision in modeling the early evolution of SNe Ia light curves is deciding what is meant by "early." While the simplistic power-law models adopted here and elsewhere can describe the flux of SNe Ia shortly after explosion, it is obvious that these models cannot explain the full evolution of SNe Ia as they never turn over and decay. Throughout the literature there are various definitions of early, ranging from some studies defining early relative to the amount of time that has passed following the epoch of discovery (e.g., Nugent et al. 2011; Zheng et al. 2013; Miller et al. 2018), to others defining it relative to the time of B-band maximum (e.g., Riess et al. 1999; Aldering et al. 2000; Conley et al. 2006; Dimi-

triadis et al. 2019), while others define early in terms of the fractional flux relative to maximum light (e.g., Olling et al. 2015; Firth et al. 2015; Fausnaugh et al. 2019). Here we adopt the latter definition to be consistent with recent work using extremely high-cadence, high-precision light curves from the space-based *Kepler* K2 (Howell et al. 2014) and the Transiting Exoplanet Survey Satellite (*TESS*; Ricker et al. 2015) missions (e.g., Olling et al. 2015; Fausnaugh et al. 2019). As in Olling et al. (2015), we only include observations up to 40% of the peak amplitude of the SN.[4] We find that this particular choice, 40% instead of 30% or 50%, does slightly affect the final inference for the model parameters (see for C.1 further details).

Of the 127 SNe Ia in our sample, we find that the MCMC chains converge for every SNe but one, ZTF18aaqnrum (SN 2018bhs). Nevertheless, we retain it in our sample as $n_{\rm steps} \approx 81\,\tau$ after 3 million steps, suggesting several independent samples within the chains (this SN is later excluded from the sample, see Appendix B). From the MCMC chains we can derive constraints on $t_{\rm fl}$, α_g, and α_r. We show example corner plots illustrating good, typical, and poor constraints on the model parameters in Figures 1, 2, and 3, respectively. In this context good, typical, and poor are defined relative to the width of the 90% credible region for $t_{\rm fl}$ (CR$_{90}$). Roughly, the good models have CR$_{90} \lesssim 1.5$ d (approximately 34 SNe), the median models have CR$_{90} \approx 2.5$ d ($\sim$61 SNe), and the poor models have CR$_{90} \gtrsim 4$ d ($\sim$32 SNe). From the corner plots it is clear that there is a positive correlation between α_g and α_r, which makes sense given the relatively similar regions of the spectral energy distribution (SED) traced by these filters. Finally, $t_{\rm fl}$ exhibits significant covariance with each of the α parameters. While we report marginalized credible regions on all model parameters in Table 2, the full posterior samples should be used for any analysis utilizing the results of our model fitting.

The bottom panels of Figures 1, 2, and 3 display the light curves for the corresponding corner plots shown in the top panels. In addition to the data, we also show multiple models based on random draws from the posterior, and the residuals normalized by their uncertainties (pull) of the data relative to the maximum a posteriori

---

[4] We do this separately in the $g_{\rm ZTF}$ and $r_{\rm ZTF}$ filters. In practice, we subtract a preliminary estimate of the flux baseline derived from the median flux value for all observations that occurred > 20 d (in the SN rest frame) before $t_{B,\rm max}$. We then divide all flux values by the peak flux determined in Yao et al. (2019). Finally, we calculate the inverse-variance weighted mean flux for every night of observations, and only retain those nights with $f_{\rm mean} \leq 0.4 f_{\rm max}$ for model fitting.
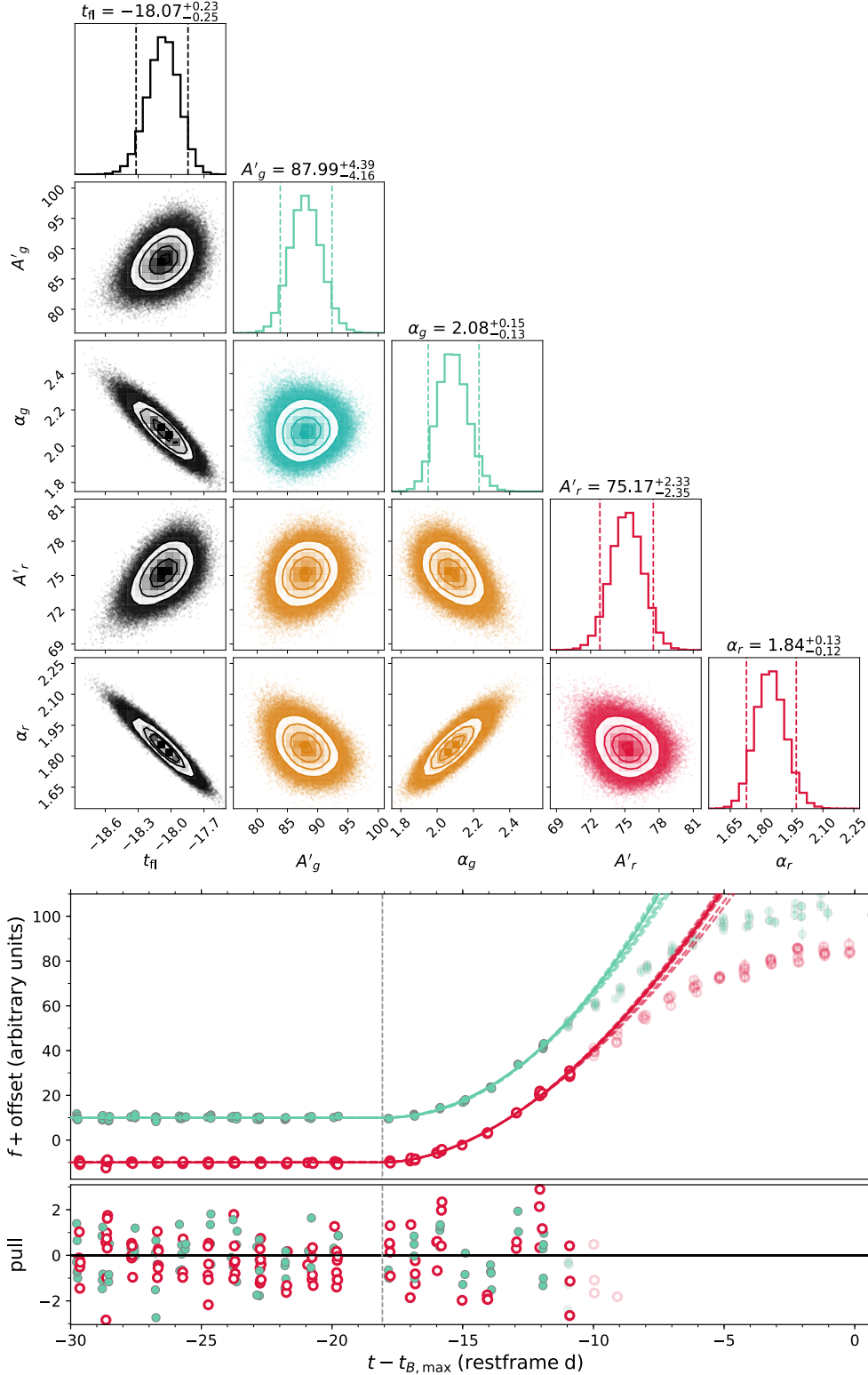
Figure 1. *Top*: Corner plot showing the posterior constraints on $t_{\rm fl}$, α_g, α_r, and the respective constants of proportionality, A'_g and A'_r for ZTF18abgmcmv (SN 2018eay). ZTF18abgmcmv is a SN that is well fit by the model. For clarity, the C_d and β_d terms are excluded (in general they do not exhibit strong covariance with the parameters shown here as they are tightly constrained by the pre-SN observations). Marginalized one-dimensional distributions are shown along the diagonal, along with the median estimate and the 90% credible region (shown with vertical dashed lines). *Bottom*: ZTF light curve for ZTF18abgmcmv showing the $g_{\rm ZTF}$ (filled, green circles) and $r_{\rm ZTF}$ (open, red circles) evolution of the SN in the month prior to $t_{B,\rm max}$. Observations included in the model fitting (i.e., those with $f \leq 0.4 f_{\rm max}$) are dark and solid, while those that are not included are faint and semi-transparent. The maximum a posteriori model is shown via a thick solid line, while random draws from the posterior are shown with semi-transparent dashed lines. The vertical dashed line shows the median 1-D marginalized posterior value of $t_{\rm fl}$, while the thin, light grey vertical line shows $t_{\rm fl}$ for the maximum a posteriori model. The bottom panel shows residuals normalized by their uncertainties (pull) relative to the maximum a posteriori model, where the factor β_d has been included in the calculation of the residuals.
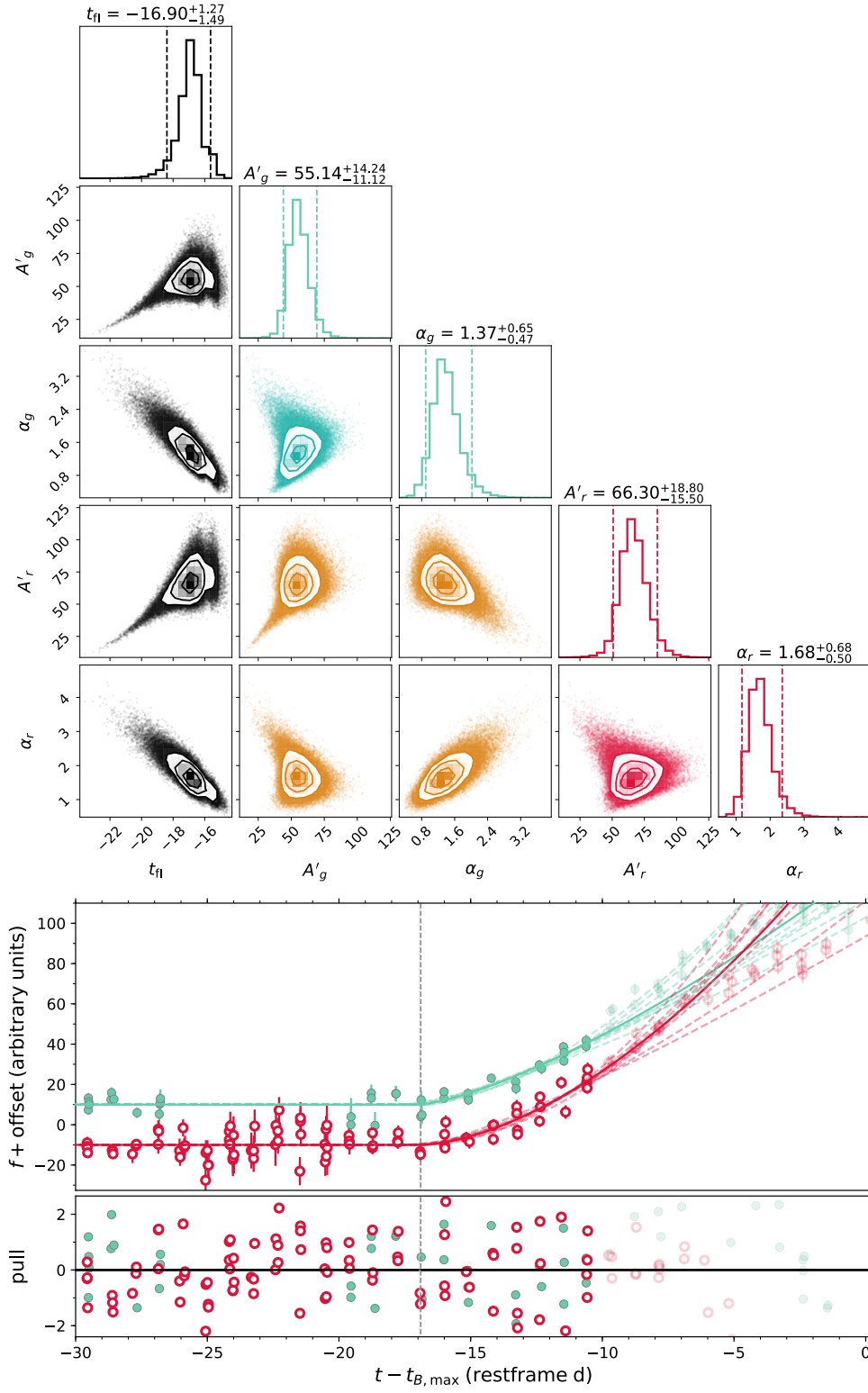
Figure 2. Same as Figure 1 for ZTF18abukmty (SN 2018lpz), a typical SN in our sample.
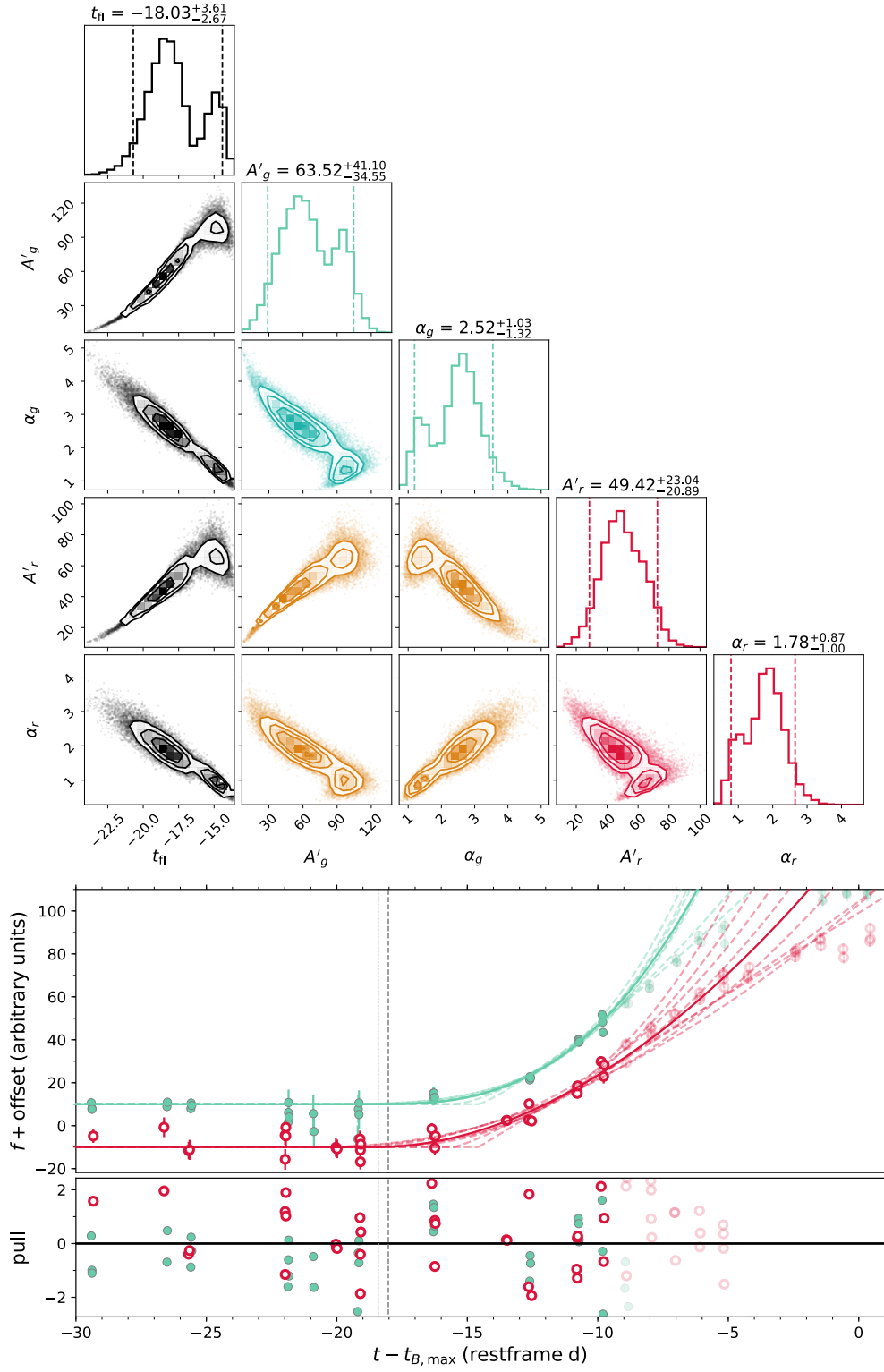
Figure 3. Same as Figure 1 for ZTF18aazabmh (SN 2018crr), a SN that does not significantly constrain the model parameters.

estimate from the MCMC sampling. As illustrated in Figure 1, we can place tight constraints on the model parameters for light curves with a high SNR. These SNe are typically found at low redshift, monitored with good sampling and at high photometric precision. As expected, as the SNR decreases (Figure 2) or the typical interval between observations increases (Figure 3), it becomes more and more difficult to place meaningful constraints on $t_{\rm fl}$ or α. We visually examine posterior models for each light curve and flag those that produce unreliable parameter constraints. We use this subset of sources to identify SNe that should be excluded from the full sample analysis described in §4 below (see Appendix B). These flagged sources are noted in Table 2.
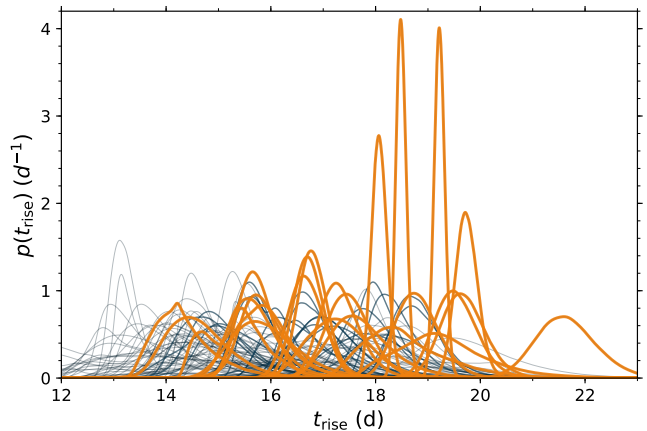
4. The Mean Rise Time and Power-Law Index for SNe Ia

Below we examine the results from our model fitting procedure to investigate several photometric properties of *normal* SNe Ia. We define normal via the spectroscopic classifications presented in Yao et al. (2019). SNe classified as SN 1986G-like, SN 2002cx-like, Ia-CSM, and super-Chandrasekhar explosions are excluded from the analysis below. These 7 peculiar events are discussed in detail in §8. The remaining 120 normal SNe Ia in our sample have $-2 \lesssim x_1 \lesssim 2$, where x_1 is the SALT2 shape parameter, which is well within the range of SNe that are typically used for cosmography (e.g., Scolnic et al. 2018). Estimates of $t_{\rm rise}$ and α for all SNe in our sample, including the 7 peculiar SNe Ia discussed in §8, are presented in Table 2.

4.1. Mean Rise Time of SNe Ia

From the marginalized 1-D posteriors for $t_{\rm fl}$, we can examine the typical rise time for SNe Ia. The model given in Equation 1 constrains $t_{\rm fl}$, yet we ultimately care about the rise time, $t_{\rm rise}$. $t_{\rm fl}$ is measured relative to $t_{B,\max}$, which itself has some measurement uncertainty.[5] An estimate of $t_{\rm rise}$ must therefore account for the uncertainties on both $t_{\rm fl}$ and $t_{B,\max}$. Aldering et al. (2000) critically showed that ignoring the uncertainties on the time of maximum could lead to $t_{\rm rise}$ estimates that are incorrect by $\gtrsim 2\,$d.

To measure $t_{\rm rise}$, we use a Gaussian kernel density estimation (KDE) to approximate the 1-D marginalized probability density function (PDF) for $t_{\rm fl}$. The width of the kernel is determined via cross validation and the KDE is implemented with `scikit-learn` (Pe-

---

[5] In this study $t_{\rm rise}$ represents the rise time to B-band maximum, as we measure time relative to $t_{B,\max}$ and assume $t_{\rm fl}$ is the same in the B, $g_{\rm ZTF}$, and $r_{\rm ZTF}$ filters (see §3).
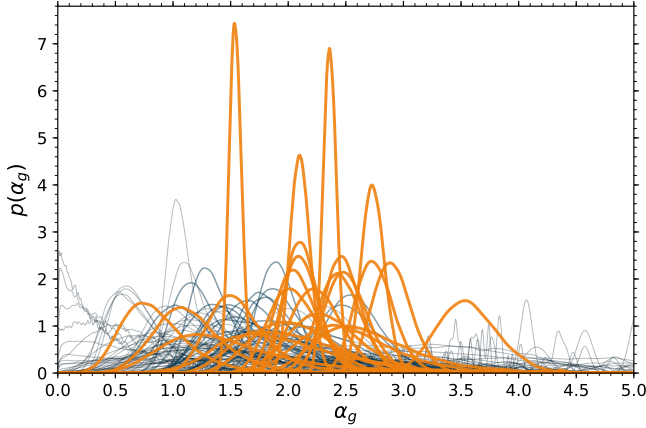

Figure 4. Marginalized posterior distribution of the rise time $t_{\rm rise}$ for normal SNe Ia in our sample. The sample has been divided into three groups (as described in the text): thin grey lines show SNe from the unreliable group (see Appendix B), dark blue lines show SNe from the reliable-$z_{\rm SN}$ group, and thick, orange lines show SNe from the reliable-$z_{\rm host}$ group. From the individual PDFs it is clear that there is no support for a single mean $t_{\rm rise}$ to describe every SN in the sample.

dregosa et al. 2011). The PDF is multiplied by -1 and convolved with a Gaussian with the same variance as the uncertainties on $t_{B,\max}$ to determine the final PDF for $t_{\rm rise}$. The cumulative density function (CDF) of this PDF is used to determine the median and 90% credible region on $t_{\rm rise}$. We assume there is no significant covariance in the uncertainties on $t_{\rm fl}$ and $t_{B,\max}$. These times are estimated using independent methods and portions of the light curve, which is why we can convolve the uncertainties in making the final estimation of $t_{\rm rise}$.

In Figure 4 we show the PDF for $t_{\rm rise}$ for the 120 normal SNe in our sample. We highlight three subsets of the normal SNe in Figure 4: SNe with reliable model parameters (see Appendix B) and known host galaxy redshifts (hereafter the reliable-$z_{\rm host}$ group), SNe with reliable model parameters and unknown host galaxy redshifts (hereafter the reliable-$z_{\rm SN}$ group; the reliable-$z_{\rm host}$ and reliable-$z_{\rm SN}$ groups together form the reliable group), and SNe with large uncertainties in the model parameters, typically due to sparse sampling around $t_{\rm fl}$ or low photometric precision (hereafter the unreliable group).

Figure 4 shows that $t_{\rm rise}$ is typically several days shorter for SNe in the unreliable group relative to SNe in the reliable group. This provides another indication that the low-quality light curves in our sample are insufficient for constraining the model parameters. Figure 4 also reveals that the rise time among individual SNe does not tend towards a common mean value. If all SNe Ia could be described with a single rise time, we could estimate that mean value by multiplying together each

Figure 5. Marginalized posterior distribution of the rising power-law index in the g_{ZTF}-band, α_g, assuming a flat prior on α_g for individual SNe in our sample. The color scheme is the same as in Figure 4. While the density of the PDFs tends towards 2, there is no support for a single mean power-law index to describe all SNe Ia.

of the PDFs shown in Figure 4. The product of the individual PDFs provides no support for a single rise time to describe all SNe Ia (i.e., it is effectively equal to 0 everywhere).

As a population, SNe Ia have a mean $t_{\mathrm{rise}} \approx 17.4\,\mathrm{d}$, where we have estimated this value by taking a weighted mean of the median value of the t_{rise} PDFs, with weights equal to the square of the inverse of the 68% credible region. The mean t_{rise} increases to $\approx 18.0\,\mathrm{d}$ and $18.3\,\mathrm{d}$ when considering only the reliable and reliable-z_{host} sub-samples, respectively (see Table 3). The scatter, estimated via the sample standard deviation, about these mean values is $\sim$1.8 d.

4.2. Mean Power-Law Index of the Early Rise

We use a similar procedure to report the PDF of α_g and α_r under the assumption of a flat prior. The posterior samples for α shown in Figure 1, 2, and 3 include a factor of $10^{-\alpha}$ following the change of variables from A to A' (see Table 1 and Appendix B). To remove this factor, we estimate the 1-D marginalized PDF of α using a KDE as above. This PDF is then divided by $10^{-\alpha}$, and then re-normalized to integrate to 1 on the interval from 0 to 10. This final normalized PDF provides an estimate of α_g and α_r assuming a $\mathcal{U}(0, 10)$ prior.

The PDFs for α_g for normal SNe Ia are shown in Figure 5. The tightest constraints on α_g come from the reliable-z_{host} group, which are clustered around $\alpha_g \approx 2$. There are, however, individual reliable-z_{host} SNe that provide support for α_g as low as $\sim$0.7 and as high as $\sim$3.5, meaning α_g can take on a wide range of values.

The weighted sample mean is $\alpha_g \approx 1.9$ for normal SNe Ia in the ZTF sample. This value increases to $\sim$2.1

when reducing the sample to the reliable group or the reliable-z_{host} group. The population scatter is $\sim$0.6 (see Table 3). For α_r the weighted sample mean is $\sim$1.7, $\sim$1.9, and $\sim$2.0 for the full sample, the reliable group, and reliable-z_{host} group, respectively. The typical scatter in α_r is 0.5 (see Table 3). As noted in §5.1, there is a tight correlation between α_g and α_r, and thus we do not show the individual PDFs for α_r.

In both the g_{ZTF} and r_{ZTF} filters the mean rising power-law index for the initial evolution of the SN is close to 2, as might be expected in the expanding fireball model. While the mean value of α is $\sim$2, it is noteworthy that the PDF for several SNe in the reliable-z_{host} sample provide no support for $\alpha = 2$. If we multiply the individual PDFs of α_g or α_r together we find there is no support for a single mean value of α capable of explaining every SN in our sample. This suggests that models using a fixed value of α are insufficient to explain the general population of normal SNe Ia (though see also §6).

4.3. Mean Color Evolution

Here we examine the mean initial color evolution of SNe Ia, *under the assumption that the early emission from SNe Ia can correctly be described by the power-law model adopted in §3*. This analysis does not address the initial colors of SNe Ia; for a more detailed analysis of the initial colors and color evolution of SNe Ia see Paper III in this series (M. Bulla et al. 2020, submitted).

Unlike t_{rise} and α, we do find evidence for a single mean value of the early color evolution of SNe Ia, as traced by $\alpha_r - \alpha_g$. If the early evolution in the g_{ZTF} and r_{ZTF} filters is a power-law in time, then the $g_{\mathrm{ZTF}} - r_{\mathrm{ZTF}}$ color, in mag, will be proportional to $(\alpha_r - \alpha_g)\log_{10}(t - t_{\mathrm{fl}})$.

To estimate $\alpha_r - \alpha_g$ we use a similar procedure as above, however, we need to estimate the marginalized joint posterior on α_g and α_r, $\pi(\alpha_g, \alpha_r \mid t_{\mathrm{fl}}, A'_b, \beta_d)$, in order to correct the posterior estimates for the priors on α. We estimate the 2D joint posterior via a Gaussian KDE, correct this distribution for the priors on α_g and α_r, and then obtain random draws from this distribution to estimate the 1-D marginalized likelihood estimates on $\alpha_r - \alpha_g$. The PDFs for $\alpha_r - \alpha_g$ for individual SNe are shown in Figure 6.

Unlike the estimates for t_{rise} and α alone, $\alpha_r - \alpha_g$ is clearly clustered around $\sim$−0.2 for the reliable group. Multiplying these likelihoods together produces support for a single mean value of $\alpha_r - \alpha_g = -0.169 \pm 0.015$, where the uncertainties on that estimate represent the 90% credible region. The mean PDF is shown as the thick, solid black line in Figure 6. A mean value of

Table 2. 90% Credible Regions for Marginalized Model Parameters (Uninformative Prior)

ZTF Name	TNS Name	z^a	$t_{\rm rise}$ (d) 5	50	95	α_g 5	50	95	α_r 5	50	95	$\alpha_r - \alpha_g$ 5	50	95	reliable[b]	normal[c]
ZTF18aailmnv	SN 2018ebo	0.080	13.58	14.26	15.64	0.69	1.05	1.81	0.41	0.74	1.36	-0.86	-0.34	0.09	n	y
ZTF18aansqun	SN 2018dyp	0.0597	12.00	13.24	15.88	1.15	3.24	5.66	0.23	0.73	1.88	-3.06	-2.81	-1.46	n	y
ZTF18aaoxryq	SN 2018ert	0.0940	12.68	13.44	14.80	0.31	0.64	1.10	0.14	0.41	0.84	-0.65	-0.22	0.20	n	y
ZTF18aapqwyv	SN 2018bhc	0.0560	13.58	14.63	16.61	1.61	2.55	4.28	0.54	1.52	3.31	-1.98	-0.97	0.03	n	y
ZTF18aapsedq	SN 2018bgs	0.0720	17.00	17.97	19.17	1.62	2.05	2.62	1.61	3.20	5.79	-0.00	1.47	3.18	n	y
ZTF18aaqcozd	SN 2018bjc	0.0732	10.33	11.62	16.02	0.56	2.28	4.61	1.13	3.47	5.46	0.63	0.81	0.99	n	y
ZTF18aaqcqkv	SN 2018lpc	0.1174	12.52	14.14	15.35	0.62	2.51	5.21	0.21	1.64	3.69	-1.74	0.80	1.82	n	y
ZTF18aaqcqvr	SN 2018bvg	0.0716	13.12	13.74	15.05	0.41	0.69	1.32	0.52	0.89	1.73	0.00	0.25	0.52	n	y
ZTF18aaqcugm	SN 2018bhi	0.0619	13.32	14.62	16.59	1.23	2.00	3.00	1.01	1.65	2.49	-0.74	-0.33	0.02	n	y
ZTF18aaqffyp	SN 2018bhr	0.070	11.16	15.61	19.38	0.03	0.31	1.35	0.02	0.23	1.10	-1.15	-0.06	0.83	n	y
ZTF18aaqnrum	SN 2018bhs	0.066	11.11	13.98	17.22	0.14	1.64	2.97	0.36	2.88	4.59	-2.20	0.53	2.68	n	y
ZTF18aaqqoqs	SN 2018cbh	0.082	17.50	18.04	18.87	1.08	1.33	1.72	1.06	1.39	1.88	-0.17	0.06	0.33	y	y
ZTF18aarldnh	SN 2018lpd	0.1077	13.48	14.54	16.58	1.20	2.22	4.21	0.77	1.33	2.37	-1.71	-1.20	-0.37	n	y
ZTF18aarqnje	SN 2018bvd	0.117	13.71	15.61	17.29	1.27	1.97	3.24	0.63	1.36	2.62	-1.53	-0.62	0.27	n	y
ZTF18aasdted	SN 2018big	0.0181	18.33	18.49	18.66	1.46	1.54	1.63	1.30	1.39	1.50	-0.21	-0.15	-0.09	y	y

Note— This table is available in its entirety in a machine-readable form in the online journal. A portion is shown here for guidance regarding its form and content.

The table includes the 5th, 50th, and 95th percentiles for the 4 parameters of interest: $t_{\rm rise}$, α_g, α_r, $\alpha_r - \alpha_g$. 90% credible regions are obtained by subtracting the 5th percentile from the 95th percentile. Estimates for $t_{\rm rise}$ come from $t_{\rm fl}$ while accounting for the uncertainties on $t_{B,\rm max}$, while estimates for the α parameters have been corrected to a flat prior (see text for further details).

[a] Redshifts are reported to 4 decimal places if the SN host galaxy redshift ($z_{\rm host}$) is known. Otherwise, the SN redshift ($z_{\rm SN}$) is reported to 3 decimal places (see Yao et al. 2019 for further details).

[b] Flag for SNe with reliable model parameters (see Appendix B). y = reliable group, n = unreliable group (see text).

[c] Flag for normal SNe Ia, y = normal, n = peculiar (the 7 peculiar SNe Ia in our sample are discussed in §8).

Table 3. Population Mean and Scatter For $t_{\rm rise}$ and α

Subset	Uninformative prior N	$t_{\rm rise}$ (d)	$\sigma_{t_{\rm rise}}$ (d)	α_g	σ_{α_g}	α_r	σ_{α_r}	$\alpha_r - \alpha_g$	$\sigma_{\alpha_r - \alpha_g}$	$\alpha = 2$ prior N	$t_{\rm rise}$ (d)	$\sigma_{t_{\rm rise}}$ (d)
normal	120	17.41 ± 0.04	1.81	1.89 ± 0.02	0.75	1.73 ± 0.02	0.80	-0.18 ± 0.01	0.73	120	21.03 ± 0.02	1.75
reliable	47	18.05 ± 0.05	1.60	2.05 ± 0.02	0.53	1.89 ± 0.02	0.50	-0.17 ± 0.01	0.23	115	21.03 ± 0.02	1.75
reliable-$z_{\rm host}$	25	18.29 ± 0.05	1.83	2.12 ± 0.02	0.59	1.99 ± 0.03	0.54	-0.18 ± 0.02	0.17	58	21.01 ± 0.02	1.96
Volume-limited ($z < 0.06$) subset												
normal	28	18.18 ± 0.05	2.23	2.05 ± 0.03	0.76	1.95 ± 0.03	0.67	-0.21 ± 0.01	0.86	28	21.17 ± 0.02	1.46
reliable	16	18.48 ± 0.05	1.73	2.13 ± 0.03	0.54	2.01 ± 0.03	0.52	-0.18 ± 0.02	0.08	27	21.17 ± 0.02	1.43
reliable-$z_{\rm host}$	15	18.52 ± 0.05	1.68	2.14 ± 0.03	0.51	2.02 ± 0.03	0.50	-0.18 ± 0.02	0.09	24	21.16 ± 0.02	1.47
DIC preferred		...	...	...	...	...	...	...	...	28	19.45 ± 0.03	1.37
DIC–uninformative	9	18.83 ± 0.03	1.33	2.14 ± 0.03	0.55	2.02 ± 0.03	0.52	-0.19 ± 0.02	0.08	...	...	...

Note— Table includes the weighted mean (see text), plus standard uncertainty in the weighted mean, as well as the scatter (the sample standard deviation), for the 4 parameters of interest, $t_{\rm rise}$, α_g, α_r, $\alpha_r - \alpha_g$, for the uninformative and $\alpha = 2$ priors. N is the number of SNe in each subset of the data, which are defined as follows (see text for more detailed definitions): normal – normal SNe Ia, reliable – SNe with reliable model parameters, reliable-$z_{\rm host}$ – reliable SNe with known host galaxy redshifts, DIC preferred – results from the $\alpha = 2$ prior, *unless the DIC prefers the uninformative prior* (see §6.2; only applies to $t_{\rm rise}$), DIC–uninformative – only SNe where the DIC prefers the uninformative prior (see §6.2; excludes the $\alpha = 2$ prior by construction). The volume limited subset includes only SNe with $z < 0.06$ (see §7). Note that the definition of reliable differs for the uninformative and $\alpha = 2$ priors, see Appendix B and §6, respectively.
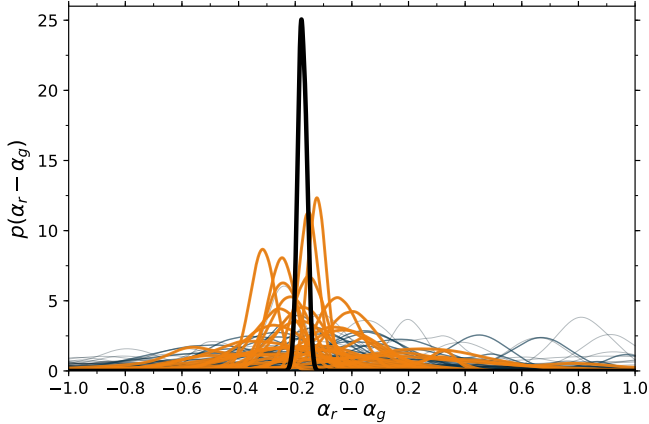
Figure 6. Marginalized posterior distribution of the early SN Ia color evolution, $\alpha_r - \alpha_g$, assuming flat priors on α_g and α_r. The color scheme is the same as in Figure 4. The thick, solid black line shows an estimate of the mean value of $\alpha_r - \alpha_g$, which is estimated by multiplying together the likelihoods for SNe *in reliable group*. There is support for a single mean value of $\alpha_r - \alpha_g \approx -0.18$ (see Table 3).

$\alpha_r - \alpha_g$ suggests that a typical, normal SN Ia becomes bluer in the days after explosion. Such an evolution makes sense for an optically thick, radioactively heated, expanding ejecta (e.g., Piro & Morozova 2016; Magee et al. 2019). There are, however, clear examples of individual SNe that do not exhibit this behavior (e.g., SN 2017cbv and iPTF 16abc; Hosseinzadeh et al. 2017; Miller et al. 2018), meaning this mean behavior is not prescriptive for every SN Ia. These results exclude SNe from the unreliable group, and their inclusion would remove any support for a single mean value of $\alpha_r - \alpha_g$. This is largely due to a small handful of events that feature extreme values of $\alpha_r - \alpha_g$ because there are gaps in the observational coverage of one of the two filters (see the upper right panel of Figure 7).

5. Population correlations

In addition to looking at the typical values of $t_{\rm rise}$ and α for SNe Ia, we also examine the correlations between these parameters, as well as how they evolve with redshift, z. These correlations may reveal details about the explosion physics of SNe Ia (for example, if strong mixing in the SN ejecta leads to low values of α, as found in Piro & Morozova 2016 and Magee et al. 2018, then any correlations with α may be related to ejecta mixing). If the model parameters are correlated with redshift, that could be evidence for either cosmic evolution of SNe Ia progenitors or inadequacies in the model.

The correlation between $t_{\rm rise}$, α_g, α_r, and z is shown in Figure 7. We do not show the correlation between α_r and z or between α_g and $t_{\rm rise}$, as this information is

effectively redundant given the tight correlation between α_g and α_r (top right panel of Figure 7).

5.1. Correlation Between α_g and α_r

The most striking feature in Figure 7 is the tight correlation between α_g and α_r. This result is reasonable because the SN SED is approximately a black body, and the $g_{\rm ZTF}$ and $r_{\rm ZTF}$ filters are relatively line free (compared to the UV) and sample adjacent portions of the Rayleigh-Jeans tail. Thus the evolution should be nearly identical in the two filters. SNe with reliable model parameters follow a tight locus around $\alpha_r - \alpha_g \approx -0.2$, with the only major outliers from this relation being SNe in the unreliable group.

The Spearman rank-ordered correlation coefficient for α_g and α_r is highly significant for the entire population ($\rho > 0.5$). Restricting the sample to SNe with reliable model parameters increases the significance of the correlation dramatically ($\rho > 0.9$). Thus, knowledge of the power-law index in either filter provides a strong predictor for the power-law index in the other filter.

5.2. Correlations with Redshift – Systematics, Not Cosmic Evolution

While less prominent, Figure 7 additionally shows that both $t_{\rm rise}$ and α are correlated with redshift. This result is somewhat surprising: naively, it suggests some form of cosmic evolution in SNe Ia, with SNe at $z \approx 0.08$ having rise times that are several days shorter than SNe at $z \approx 0.02$. The small range of redshifts in our sample, and several previous studies (e.g., Aldering et al. 2000; Conley et al. 2006; Jones et al. 2019), render this naive explanation in doubt. Instead, these correlations are the result of building a sample from a flux-limited survey.

Given that ZTF cannot detect SNe when their observed brightness is $g_{\rm ZTF} \gtrsim 21.5$ mag (Masci et al. 2019; Bellm et al. 2019a), SNe at progressively higher redshifts are discovered at a later phase in their evolution. The large degeneracies in the model presented in Equation 1, namely between $t_{\rm fl}$, A, and α, allow for a great deal of flexibility when fitting the data. For SNe discovered at later phases, it is possible to adjust $t_{\rm fl}$ while decreasing A and α, such that $t_{\rm fl}$ occurs around the epoch of first detection (resulting in a shorter rise time).

We illustrate this effect in Figure 8, which shows that the inferred rise time for identical SNe decreases as those SNe are observed at successively higher redshifts. We use the 4 normal SNe with $z \leq 0.03$ and simulate their appearance at higher redshift by making the (over-simplified) assumption that all detections are in the sky-background dominated regime. Thus, in any given epoch the SNR $\propto d_L^{-2}$, where d_L is the SN luminosity distance. To simulate the SN at some new redshift,
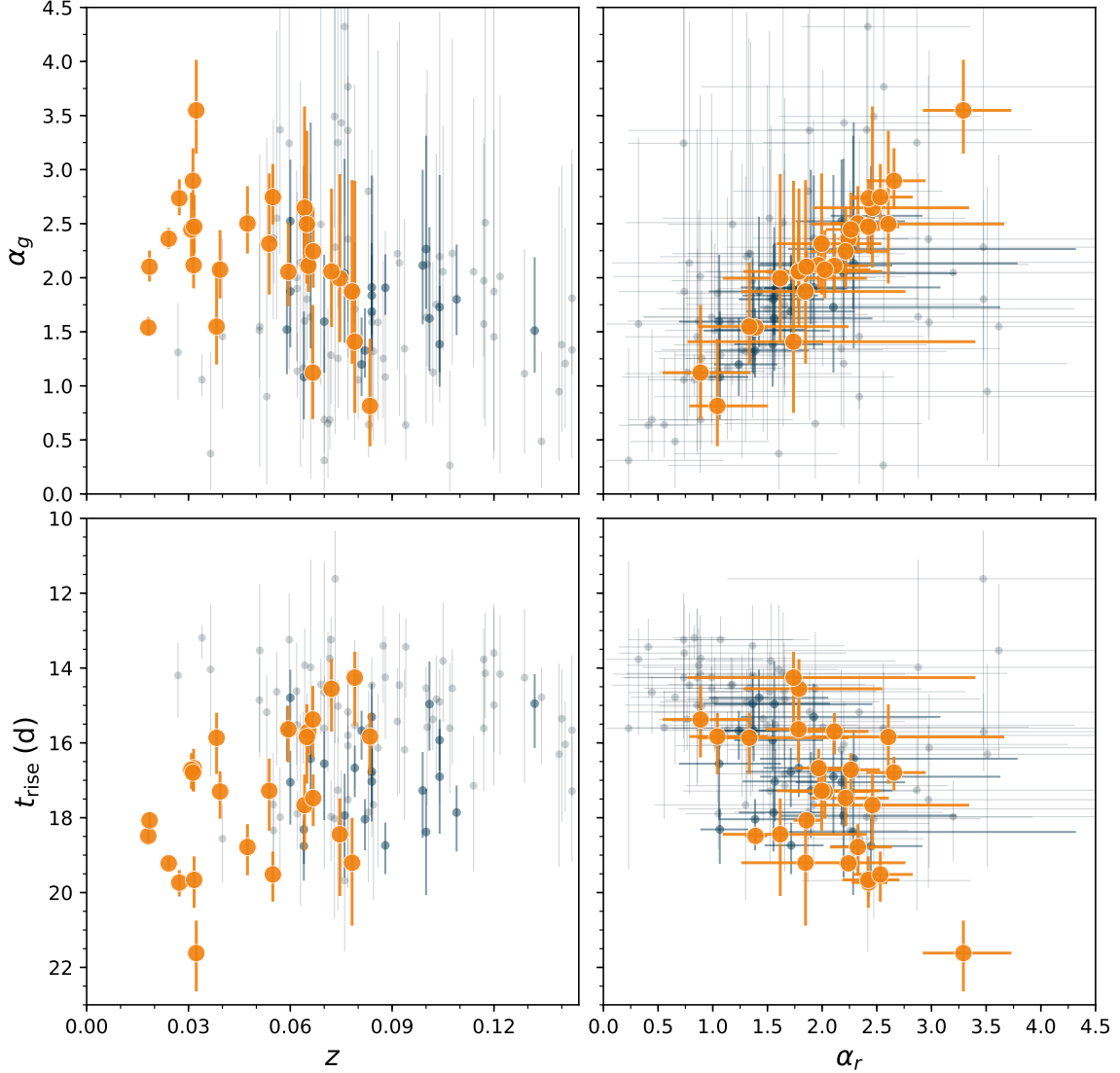
Figure 7. Correlation between redshift, z, SN rise time, $t_{\rm rise}$, and the power-law index in the $g_{\rm ZTF}$ and $r_{\rm ZTF}$ filters, α_g and α_r, respectively. We do not show α_r vs. z or $t_{\rm rise}$ vs. α_g, as these would largely be redundant given the very strong correlation between α_g and α_r (upper right panel). The sample has been divided into three groups: small, light grey circles show SNe from the unreliable group (see Appendix B), dark blue circles show the reliable-$z_{\rm SN}$ group, and large orange circles show the reliable-$z_{\rm host}$ group. The plots show that redshift is correlated with both $t_{\rm rise}$ and α_g, which would only be expected if SNe Ia undergo significant evolution from $z \approx 0$ to 0.1. We later show this to be the result of a systematic selection effect (see text for further details).

$z_{\rm sim}$, we multiply the uncertainties by $(d_{L,{\rm sim}}/d_{L,{\rm obs}})^2$, where $d_{L,{\rm sim}}$ is the luminosity distance at $z_{\rm sim}$, and $d_{L,{\rm obs}}$ is the observed luminosity distance to the SN.[6] Using these increased uncertainties, we randomly resample the observed flux values from a normal distribution with mean equal to the original flux and variance equal

to the square of the distance-scaled uncertainty. After correcting the observation times to the simulated rest frame, we fit the noisier simulated data with the procedure from §3. We simulate the appearance of these SNe at redshifts $z = 0.05$, 0.075, 0.1, and 0.15. Only the models that converge are shown in Figure 8.

The results shown in Figure 8 are clear: SNe discovered at higher redshifts have systematically smaller estimates for $t_{\rm rise}$. This result is simple to understand as higher redshift SNe will not be detected until later in

---

[6] Following Yao et al. (2019), we adopt a flat ΛCDM cosmology with $H_0 = 73.24\,{\rm km\,s^{-1}\,Mpc^{-1}}$ (Riess et al. 2016) and $\Omega_m = 0.275$ (Amanullah et al. 2010) to calculate d_L for the SNe.
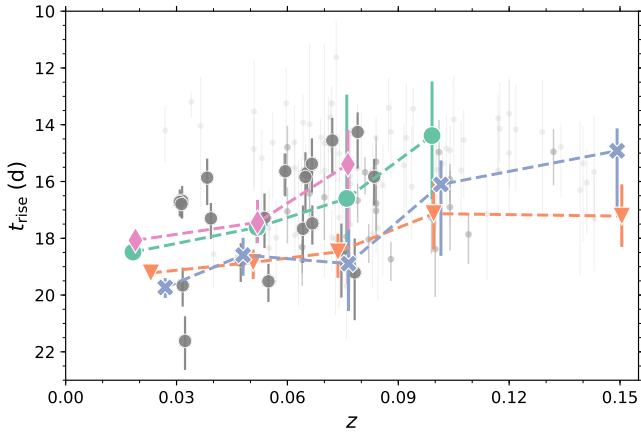
Figure 8. Same as the bottom left panel of Figure 7, though all SNe are shown in grey. The large green circle, magenta diamond, orange triangle, and purple X show how marginalized posterior estimates of $t_{\rm rise}$ change as the four lowest redshift SNe are observed at $z = 0.05$, 0.075, 0.1, and 0.15 (see text for further details). For clarity, slight offsets in z have been applied to the symbols, as the error bars would otherwise fully overlap. $t_{\rm rise}$ clearly decreases with increasing redshift, showing that the observed correlation between these parameters is a consequence of flux-limited SN surveys.

their evolution. A stronger prior on any of the model parameters would help to combat this effect (see §6), though as previously discussed we avoid strong priors due to the wide range of α and $t_{\rm fl}$ that has been reported in the literature.

This effect also explains the correlation seen in the bottom right panel of Figure 7. SNe detected later in their evolution will be evolving less rapidly as the rate of change in brightness continually decreases until the time of maximum light. Hence, a later detection provides a lower value of α. Indeed, a re-creation of Figure 8 showing α_g instead of $t_{\rm rise}$ shows α_g decreasing with increasing redshift. Thus, the observed correlations with redshift seen in Figure 7 can be entirely understood as the result of ZTF being a flux-limited survey.

The implications of this result have consequences well beyond the ZTF sample discussed here. Essentially all SN surveys are flux-limited, meaning the systematics associated with redshift will affect any efforts to determine $t_{\rm rise}$ or α in those data as well. The inclusion of higher-redshift SNe in the sample will, on average, bias estimates of $t_{\rm rise}$ and α to lower values. Even more concerning is the possibility that this trend may continue to very low redshifts ($z \ll 0.01$). The paucity of SNe in this redshift range, due to the relatively small volume probed, make it difficult to test for such an effect. Due to the systematic identified here, it may be the case that the rise time, and by extension also α, are underestimated for every SN in the literature. Detailed simu-

lations with realistic SN light curves are needed to test this possibility.

5.3. Correlations with Light Curve Shape

A defining characteristic of SNe Ia is that they can be described by a relatively simple luminosity-shape relation (Phillips 1993), which enables them to be used as standardizable candles. We examine the correlation between light curve shape, in this case the SALT2 x_1 parameter, and the SN rise time and α in Figure 9. There is a clear correlation between shape and $t_{\rm rise}$, which has been hinted at in other smaller samples (e.g., Riess et al. 1999; Firth et al. 2015; Zheng et al. 2017). The Spearman coefficient for x_1 and $t_{\rm rise}$ is significant for the entire population ($\rho > 0.4$), and increases when considering the reliable-$z_{\rm host}$ group ($\rho > 0.6$).

An observed correlation between x_1 and $t_{\rm rise}$ should be expected as the x_1 shape parameter accounts for the width of both the SN rise and decline, and therefore, by definition, should be correlated with the rise time. The middle and right panels of Figure 9 divide the reliable-$z_{\rm host}$ group into low ($z < 0.06$) and high ($z \geq 0.06$) redshift bins. From these panels it is clear that some of the scatter in the x_1–$t_{\rm rise}$ plane is the result of the redshift bias discussed in §5.2, as higher redshift SNe have shorter rise times at fixed x_1. A correction for this redshift effect would reduce the overall scatter seen in the lower panels of Figure 9 (see §6 for a method to reduce this bias).

We compare independent measurements of the rise time and decline of SNe Ia in Figure 10, which shows the correlation between $t_{\rm rise}$ and $\Delta m_{15}(g_{\rm ZTF})$, the observed decline in magnitudes of the $g_{\rm ZTF}$ light curve between the time of maximum light and 15 d later. $\Delta m_{15}(g_{\rm ZTF})$ is measured via low-order polynomial fits to the $g_{\rm ZTF}$ photometry from phase $= -5$ to $+20$ d. For 15 of the 127 SNe in our sample this measurement is not possible due to an insufficient number of observations in the defined window. We additionally exclude 6 SNe from Figure 10 where the relative uncertainty on $\Delta m_{15}(g_{\rm ZTF})$ is greater than 25%. Figure 10 shows that, on average, slowly declining SNe with smaller values of $\Delta m_{15}(g_{\rm ZTF})$ have longer rise times (Spearman $\rho \approx -0.35$ for the full sample, and ~ -0.6 for the reliable-$z_{\rm host}$ group). Furthermore, as was the case for x_1, Figure 10 shows that at least some of the scatter in this relation can be explained as a redshift effect because SNe at higher redshift have shorter rise times, on average, for a fixed value of $\Delta m_{15}(g_{\rm ZTF})$.

The observed correlation between the rise time and the SN decline rate stands in contrast to what was found in Hayden et al. (2010), where the slowest declining SNe
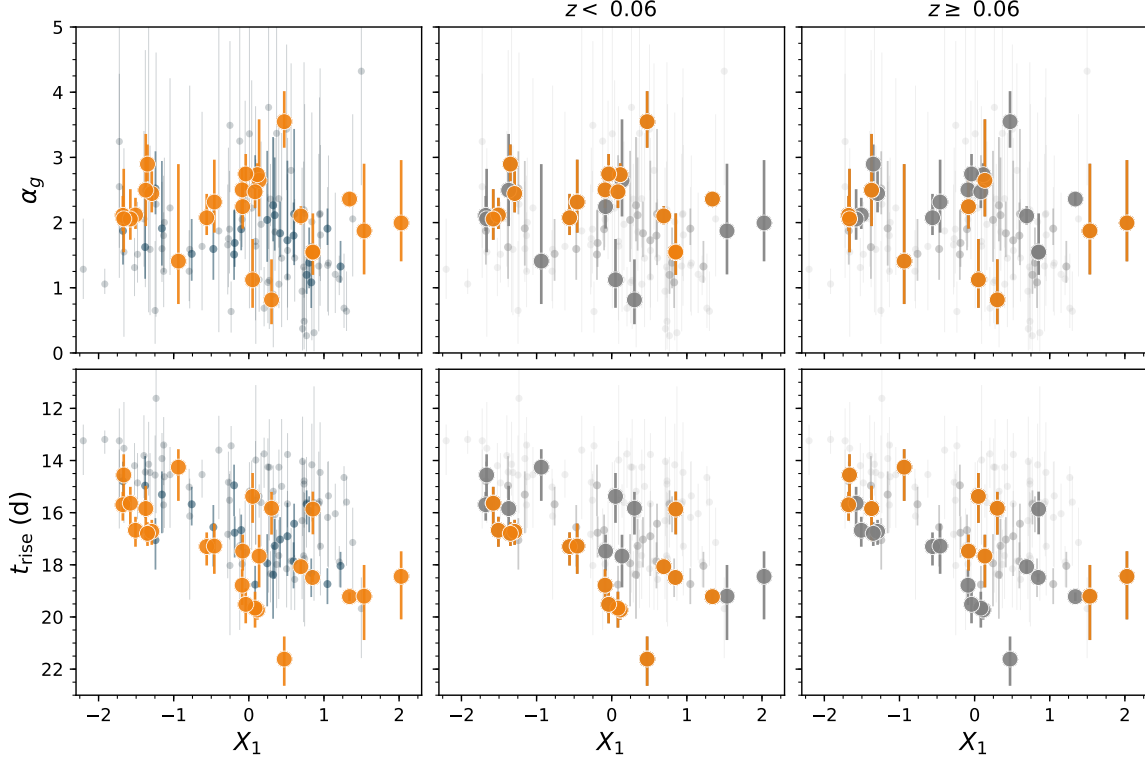
Figure 9. Correlation between the `SALT2` x_1 shape parameter and α_g (top row) and $t_{\rm rise}$ (bottom row). Symbols are the same as Figure 7. For clarity, the uncertainties on x_1 are not shown. $t_{\rm rise}$ shows a strong correlation with x_1, while there is no correlation between α_g and x_1. The middle and right panels highlight reliable-$z_{\rm host}$ SNe at low, $z < 0.06$, and high, $z \geq 0.06$, redshift, respectively. Dividing the sample into different redshift bins shows that some of the observed scatter between x_1 and the model parameters is due to redshift and not intrinsic scatter.
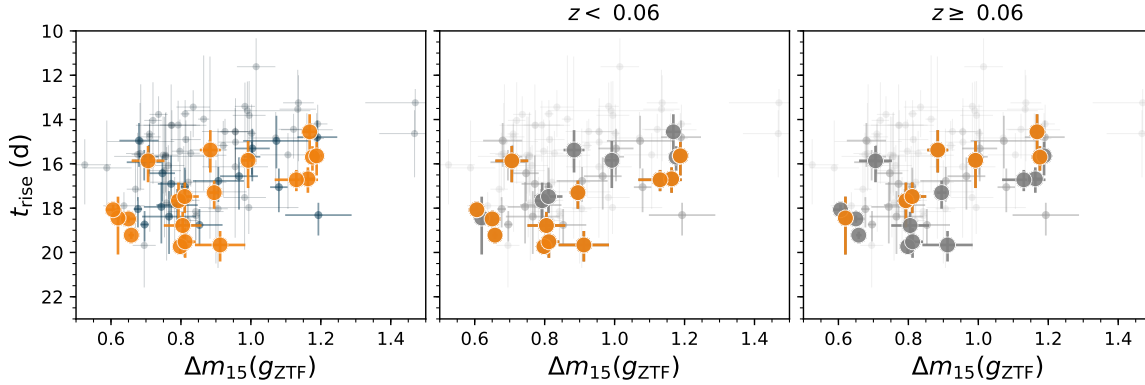
Figure 10. Correlation between $\Delta m_{15}(g_{\rm ZTF})$ and $t_{\rm rise}$. Symbols are the same as Figure 7. There is a clear correlation between the rise and decline times of SNe Ia. Some of the scatter in the relationship between these parameters can be explained as a result of the redshift effect discussed in §5.2.

are among the fastest risers, and a few fast-declining SNe have long rise times. This particular result may be understood in the context described in §5.2. Slowly declining SNe are more luminous, and therefore will, on average, be found at higher redshifts than rapidly declining events in a flux-limited survey. As Figure 8 shows, rise times are underestimated for higher redshift events. Indeed, such an effect is seen in the ZTF sample,

as illustrated in the 2 right columns of Figure 9. If the reliable-$z_{\rm host}$ subsample is divided in redshift bins, it is clear that, at fixed values of x_1, the corresponding value of $t_{\rm rise}$ decreases as the redshift increases. This bolsters the arguments in §5.2 that there is a systematic error in the estimate of $t_{\rm rise}$ due to redshift, and means that the intrinsic scatter in the relation between x_1 and $t_{\rm rise}$ is much smaller than the observed scatter seen in Figure 9.

There is no strong correlation between α and x_1 (Figure 9). The Spearman correlation for these two parameters is $\rho \approx -0.2$ whether looking at α_g or α_r, or whether considering the full sample, the reliable group, or the reliable-z_{host} group. Subdividing the reliable-z_{host} group by redshift shows the same trend that was identified in Figure 7: higher redshift SNe have smaller values of α on average for the reliable-z_{host} group.

6. Strong Priors

6.1. Fixing $\alpha = 2$

In our previous effort to model the early evolution of SNe Ia we adopted a flexible model (hereafter the "uninformative prior") allowing α and t_{fl} to simultaneously vary, despite theoretical (Arnett 1982; Riess et al. 1999) and observational (Conley et al. 2006; Hayden et al. 2010; Ganeshalingam et al. 2011) evidence that α is consistent with 2. Here we alter the model by fixing $\alpha_g = \alpha_r = 2$ (hereafter the "$\alpha = 2$ prior"), and explore how this decision changes the results described in the previous sections. This decision is equivalent to placing an infinitely strong prior on the value of α.[7]

The distribution of rise time PDFs using the $\alpha = 2$ prior is shown in Figure 11, and reported in Table 4. Adopting this strict prior significantly reduces the flexibility of the model. One consequence of this choice is that visual inspection of the posterior predictive flux values reveals that there are far fewer SNe with unreliable model parameters. When using the $\alpha = 2$ prior, we only flag SNe with an extrapolated flux using the maximum a posteriori model parameters $< 0.9f_{max}$ at $t_{B,max}$ as having unreliable model parameters. From this criterion only 5 SNe are flagged as having unreliable model parameters.

Figure 11 shows rise times that are significantly longer, on average ~ 3 d, than those inferred from the uninformative prior (see Figure 4). Adopting the $\alpha = 2$ prior leads to far more SNe with narrow PDFs for t_{rise}. Multiplying the individual likelihoods for t_{rise} does not provide support for a single mean rise time. Following the same approach described in §4.1, we find a population mean $t_{rise} \approx 21.0$ d, with a corresponding population scatter of ~ 1.8 d for the $\alpha = 2$ prior (see Table 3). Another consequence of adopting the $\alpha = 2$ prior is that a small handful (~ 5–6) of SNe have rise times consistent with 26 d, which is considerably longer than the

---

[7] Strictly enforcing $\alpha_g = \alpha_r$ imposes non-physical structure on the models, as this condition effectively implies that there is no change in the $g - r$ colors during the initial rise of the SN. This is clearly observed not to be the case in many SNe (§4.3; see also Paper III in this series, M. Bulla et al. 2020, submitted).

Table 4. 90% Credible Region for t_{rise} ($\alpha = 2$ Prior)

ZTF Name	TNS Name	t_{rise} (d) 5	50	95	reliable[a]
ZTF18aailmnv	SN 2018ebo	20.19	21.40	22.84	y
ZTF18aansqun	SN 2018dyp	17.26	18.66	20.32	y
ZTF18aaoxryq	SN 2018ert	20.24	22.44	25.57	y
ZTF18aapqwyv	SN 2018bhc	17.28	18.40	19.98	y
ZTF18aapsedq	SN 2018bgs	21.01	21.67	22.33	y
ZTF18aaqcozd	SN 2018bjc	17.48	18.95	20.88	y
ZTF18aaqcqkv	SN 2018lpc	16.81	18.99	21.32	n
ZTF18aaqcqvr	SN 2018bvg	20.47	21.26	22.20	y
ZTF18aaqcugm	SN 2018bhi	18.47	18.93	19.45	y
ZTF18aaqffyp	SN 2018bhr	17.15	22.61	26.03	n
ZTF18aaqnrum	SN 2018bhs	15.80	21.89	24.85	y
ZTF18aaqqoqs	SN 2018cbh	23.14	23.62	24.11	y
ZTF18aarldnh	SN 2018lpd	18.58	19.83	21.30	y
ZTF18aarqnje	SN 2018bvd	19.23	20.38	21.66	y
ZTF18aasdted	SN 2018big	22.89	23.00	23.12	y

NOTE— This table is available in its entirety in a machine-readable form in the online journal. A portion is shown here for guidance regarding its form and content.

The table includes the 5th, 50th, and 95th percentiles for t_{rise} after adopting the $\alpha = 2$ prior (see text for further details).

[a] Flag for SNe with reliable model parameters. Note that the $\alpha = 2$ prior definition of reliable differs from that in Appendix B (see text).
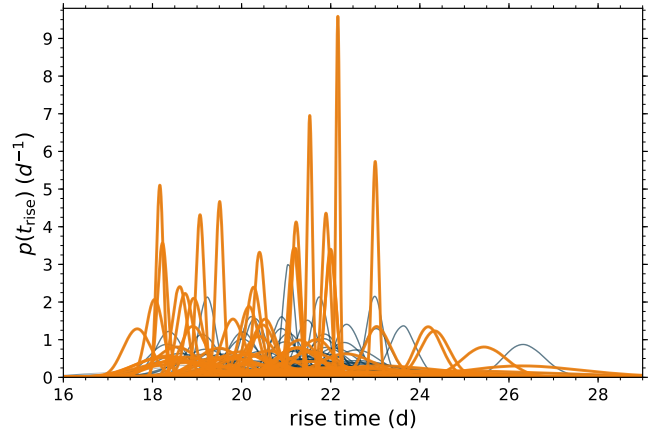
Figure 11. Same as Figure 4, showing the resulting PDFs for the $\alpha = 2$ prior. Note that the definition for reliable model parameters with the $\alpha = 2$ prior is different from that described in Appendix B (see text). As was the case when α is allowed to vary, there is no support for a single mean t_{rise} to describe every SN in the sample. The $\alpha = 2$ prior results in rise times that are ~ 3 d longer on average.

rise times inferred in any previous study of normal SNe Ia.

Figure 12 shows t_{rise} as a function of redshift (left) and x_1 (right) when adopting the $\alpha = 2$ prior. The previously observed correlation between t_{rise} and red-

shift disappears when assuming $\alpha = 2$. The Spearman rank-order correlation coefficient for these two parameters is $\rho \lesssim 0.2$ for the full sample, and the reliable and reliable-z_{host} subsamples. The model is, in effect, no longer flexible enough to systematically adjust t_{fl} to be approximately equal to the epoch of first detection. The removal of this particular bias provides a benefit of fixing $\alpha = 2$.

Adopting the $\alpha = 2$ prior yields a significantly smaller scatter in the correlation between x_1 and t_{rise}, as shown in Figures 9 and 12. The reduction in this scatter intuitively makes sense, given that it was due, at least in part, to the redshift bias in measuring t_{rise} (§5.2). Reducing, or possibly fully removing, that bias by adopting the $\alpha = 2$ prior allows a direct estimate of the rise time from x_1 with a typical scatter $< 1\,\text{d}$. If relatively high precision measurements of t_{rise} can be directly inferred from x_1, it would dramatically increase the sample of SNe Ia with measured rise times, as extremely early observations ($t < -10\,\text{d}$) would no longer be required given that x_1 can be inferred solely from observations around and post-peak maximum light (see §9.1.1).

6.2. Model Selection

In adopting two very different priors that, in turn, produce significantly different posteriors, we are naturally left with the question: which model is better? To some extent, the answer to this question rests with every individual as the prior quantifies one's a priori belief about the model parameters. We posit that it is extremely unlikely that thermonuclear explosions all identically produce $\alpha = 2$ across a multitude of filters. Thus, adopting $\alpha = 2$ is very likely an overconfident position that produces slightly biased inference as a result.

Alternatively, we can address the question of which model is best via the use of model selection techniques based on information criteria. In our initial fit of the SN light curves we effectively included additional parameters in the model by allowing α to vary. Thus, for individual SNe, we can compare the trade-off between increasing the model complexity relative to the overall improvement in the model fit to the data, in order to determine which model is superior. Following Spiegelhalter et al. (2002), we define the deviance D as

$$D(\theta) = -2\ln(p(x \mid \theta)) + C,$$

where θ are the model parameters, x are the observations, $p(x \mid \theta)$ is the likelihood, and C is a constant that will drop out following model comparison. From here,

the effective number[8] of model parameters p_D can be calculated as:

$$p_D = \langle D(\theta) \rangle - D(\langle \theta \rangle),$$

where $\langle D(\theta) \rangle$ is the mean posterior value of the deviance, and $D(\langle \theta \rangle)$ is the deviance of the mean posterior model parameters. We then define the deviation information criterion (DIC) as:

$$\text{DIC} = p_D + \langle D(\theta) \rangle.$$

Smaller values of the DIC are preferred to larger values.

Following Jeffreys (1961) we consider SNe with

$$\exp\left(\frac{\text{DIC}_{\alpha 2} - \text{DIC}_{\text{flat}}}{2}\right) \geq 30,$$

where $\text{DIC}_{\alpha 2}$ is the DIC for the $\alpha = 2$ prior and DIC_{flat} is the DIC for the uninformative prior, to exhibit a very strong preference for the uninformative prior. Of the 127 SNe in our sample, including the 7 SNe that are not considered normal SNe Ia, only 29 show a strong preference for the uninformative prior. Of these 29 SNe, 16 belong to the unreliable group. Visual inspection of these 16 confirms that these SNe have very few detections after t_{fl}. In these cases the data are extremely well fit with very small values of α (see e.g., Figure B1). The remaining 13 SNe are at low z, with few, if any, gaps in observational coverage.

Thus, the $\alpha = 2$ prior should be used to estimate t_{fl} for all but 13 SNe in our sample. For these 13, the uninformative prior provides a better estimate of t_{fl}, according to the DIC. This combination of results is how we define the distribution of t_{fl} in Paper III of this series (M. Bulla et al. 2020, submitted).

7. A Volume Limited Sample of Normal SNe Ia

The ZTF sample of SNe Ia is clearly biased due to Malmquist selection effects (see Yao et al. 2019), and as such, the population results discussed above are also correspondingly biased. We can, however, approximate a volume limited subset of *normal* SNe Ia. A full study of the completeness of the ZTF SNe Ia sample is beyond the scope of this paper and will be discussed in a future study (J. Nordin et al., in prep.).

The selection criteria presented in Paper I removes SNe Ia from the sample if they lack a g_{ZTF} detection

---

[8] We adopt the Deviance Information Criterion, as opposed to the Akaike or Bayesian Information Criteria because our model includes many nuisance parameters that we ultimately marginalize over for our final inference. The DIC more naturally accounts for these marginalized parameters.
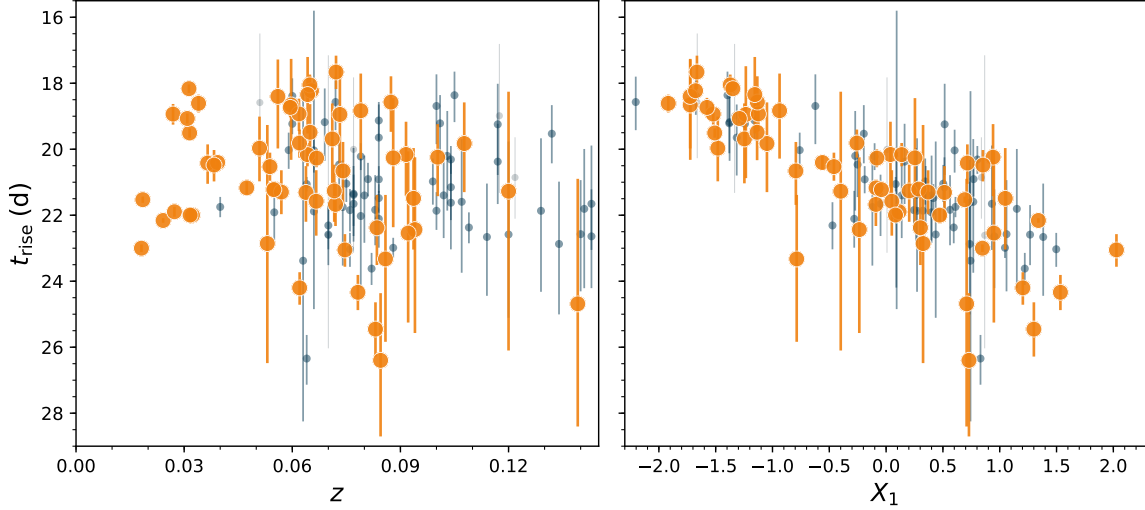
Figure 12. Correlation between $t_{\rm rise}$ and redshift (left) and x_1 (right) when adopting the $\alpha = 2$ prior for the early emission from SNe Ia. The use of this strict prior removes the previously observed bias that resulted in shorter rise times being inferred at higher redshifts. A consequence of the removal of this bias is a reduction in the observed scatter between $t_{\rm rise}$ and x_1.

> 10 d prior to $t_{B,\rm max}$ (Yao et al. 2019). By construction, the intrinsically faintest normal SNe Ia in the ZTF sample have $x_1 \approx -2$, with $M_g \approx -17$ mag at $t \approx -10$ d. With a typical limiting magnitude of $g_{\rm ztf} \approx 20.0$ mag during bright time (Bellm et al. 2019a), the ZTF high-cadence survey should be complete to all $x_1 \approx -2$ and brighter SNe to a distance modulus $\mu \approx 37$ mag. For our adopted cosmology, this distance corresponds to a redshift $z \approx 0.0585$. Thus, the 28 normal SNe Ia with $z < 0.06$ should comprise a volume-limited subset of our sample.

For the uninformative prior, 16 of the 28 low redshift SNe have reliable model parameters, and 15 of those 16 have known host redshifts. Using the same procedure as §4.1, we estimate a weighted mean rise time of $\sim$18.5 d when considering the volume complete subset ($z < 0.06$) of our sample (see Table 3 for the mean values discussed here and in the remainder of this section). For these SNe, we also find mean values of $\sim$2.13 and $\sim$2.01 for α_g and α_r, respectively.

For the $\alpha = 2$ prior, 27 of the 28 low redshift SNe have reliable model parameters, and 24 of those 27 have known host redshifts. For this prior, we estimate a weighted mean rise time of $\sim$21.2 d.

If we instead use the results from the $\alpha = 2$ prior, unless the DIC provides very strong evidence for the uninformative prior, as suggested at the end of §6.2, then we find a mean rise time of $\sim$19.5 d for the volume-limited sample. It makes sense that this mean is nearly 2 d shorter than the mean for the $\alpha = 2$ prior because the SNe for which the DIC prefers the uninformative prior provide the tightest constraints on $t_{\rm rise}$.

Finally, if we reduce the sample to only those SNe for which the DIC prefers the uninformative prior, of which there are only 9 normal SNe with $z < 0.06$ (all of which have known $z_{\rm host}$) in our entire sample, we find a mean rise time of 18.83 ± 0.03. For this same subset we find mean values of α_g and α_r of 2.14 ± 0.03 and 2.02 ± 0.03, respectively.

Given the bias identified in §5.2, it is not surprising that a volume-limited sample of SNe has larger estimates for the mean values of $t_{\rm rise}$ and α, when using the uninformative prior. For the $\alpha = 2$ prior, on the other hand, the volume-limited sample produces a very similar estimate for the mean $t_{\rm rise}$ ($< 1\%$ difference) as the full sample. This provides additional evidence that the adoption of a strong prior can negate the redshift bias highlighted in §5.2.

8. Rare and Unusual Thermonuclear SNe

In Yao et al. (2019), we identified 6 peculiar SNe Ia, which were classified as either SN 2002cx-like (hereafter 02cx-like or SN Iax), super-Chandrasekhar (SC) explosions, or SNe Ia interacting with their circumstellar medium (CSM), known as SN Ia-CSM. For this study we have also excluded ZTF18abdmgab (SN 2018lph), a 1986G-like SN that would not typically be included in a sample used for cosmological studies. Here we summarize the early evolution of these events.

For ZTF18abclfee (SN 2018cxk), an 02cx-like SN at $z = 0.029$, we obtained an exquisite sequence of observations in the time before explosion, as shown in Figure 13. According to the DIC, $\alpha \neq 2$ is decisively preferred for this SN. For ZTF18abclfee, we estimate $t_{\rm rise} = 10.01 \pm_{0.33}^{0.40}$ d (the uncertainties represent the 90%
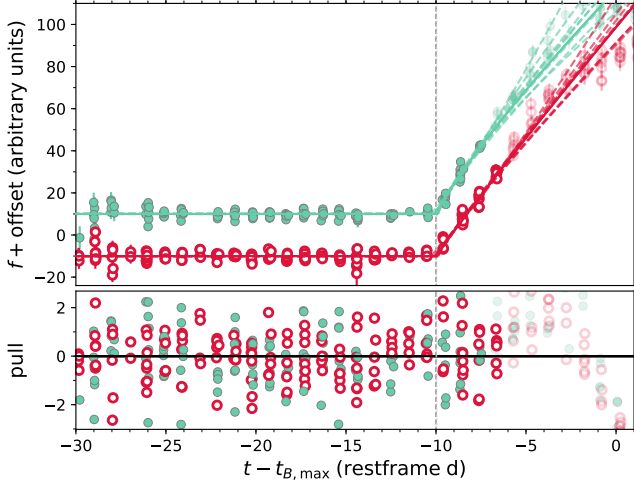
Figure 13. Same as the bottom panel of Figure 1 for ZTF18abclfee (SN 2018cxk), an 02cx-like SN with strong constraints on $t_{\rm fl}$, and a short rise time ($\sim$10 d). ZTF18abclfee has the tightest constraints on $t_{\rm rise}$ of all 02cx-like SNe observed to date.

credible region). This is the most precise measurement of the rise time of an 02cx-like SN to date. The only other 02cx-like event with good limits on the rise with deep upper limits is SN 2005hk (Phillips et al. 2007). SN 2005hk has a substantially longer rise time ($\sim$15 d; Phillips et al. 2007) than ZTF18abclfee, which is not surprising given that ZTF18abclfee is less luminous and declines more rapidly than SN 2005hk (Miller et al. 2017; Yao et al. 2019). ZTF18abclfee also exhibits a nearly linear early rise with $\alpha_g = 0.95^{+0.32}_{-0.19}$ and $\alpha_r = 0.98^{+0.23}_{-0.15}$.

ZTF18aaykjei (SN 2018crl), a Ia-CSM SN with $t_{\rm rise}=$ 22.8$\pm^{2.0}_{1.8}$ d and 26.3$\pm$1 d for the uninformative and $\alpha = 2$ priors, respectively, has a significantly longer rise than the normal SNe in this study. Silverman et al. (2013) points out that Ia-CSM have exceptionally long rise times, and Firth et al. (2015) measure $t_{\rm rise} > 30$ d for two of the SNe in the Silverman et al. (2013) sample. We also note that the $r_{\rm ZTF}$ peak of ZTF18aaykjei occurs at least one week after the $g_{\rm ZTF}$ peak, as has been seen in other Ia-CSM SNe (Aldering et al. 2006; Prieto et al. 2007).

There are two SC SNe Ia (ZTF18abdpvnd/SN 2018dvf and ZTF18abhpgje/SN 2018eul) and two candidate SC SNe (ZTF18aawpcel/SN 2018cir and ZTF18abddmrf/SN 2018dsx) identified in Yao et al. (2019). Each of these events exhibits a long rise, $\gtrsim 20$ d and $\gtrsim 25$ d for the uninformative and $\alpha = 2$ priors, respectively, as previously seen in other SC events (e.g., Scalzo et al. 2010; Silverman et al. 2011). We note that with the exception of ZTF18abdpvnd ($z = 0.05$), these events are detected at high redshift ($z \gtrsim 0.15$), and

as a result the constraints on the individual rise time measurements are relatively weak.

Finally, for ZTF18abdmgab (SN 2018lph), the 86G-like SN identified in Yao et al. (2019), we cannot place strong constraints on the rise time due to a significant gap in the observations around $t_{\rm fl}$.

9. Discussion

9.1. SNe Ia Rise Times

In the analysis above, we provide multiple measurements of the rise time of SNe Ia following the adoption of different priors. Within the literature, there are at least a half dozen entirely different methods that have been employed to answer precisely the same question. This naturally raises the question – which method is best? Which raises an important offshoot as well – is the method cheap to implement (i.e., does it provide reliable inference in the limit of poor sampling or low SNR)?

9.1.1. SALT2 x_1 as a Proxy for $t_{\rm rise}$

Estimating the rise times of SNe Ia using only observations around maximum brightness would be an ideal approach, as the required observations are relatively cheap. Such an approach would also maximize the sample size from flux-limited surveys, and Figure 12 suggests this might be feasible given the correlation between the SALT2 x_1 parameter and $t_{\rm rise}$ (measured using the $\alpha = 2$ prior).[9] Even in the limit of only one or a few observations on the rise, SALT2 can still measure x_1 (e.g., Scolnic et al. 2018). Therefore, the correlation between x_1 and $t_{\rm rise}$ eliminates the need for high-cadence observations to yield early (> 10 d prior to $t_{B,\max}$) discoveries, enabling a more economical method to estimate $t_{\rm rise}$ relative to the methods described above.

For the volume-limited sample (see §7) of normal SNe Ia with known host galaxy redshifts and reliable model parameters, we estimate the relation between $t_{\rm rise}$ and x_1 via a maximum-likelihood linear-fit that accounts for the uncertainties on both $t_{\rm rise}$ and x_1 (see Hogg et al. 2010). From this fit we find

$$t_{\rm rise} = (20.94 \pm 0.03) + (1.47 \pm 0.03)x_1 \text{ d.} \qquad (3)$$

The residual scatter about this relation, as estimated by the sample standard deviation, is 0.77 d. We find the relation does not significantly change when including SNe with unknown host-galaxy redshifts or unreliable model parameters (though the scatter increases to

---

[9] Other shape parameters, such as the stretch, s, or distance from a fiducial template, Δ, may work in place of x_1.

$\sim$1.1 d when including $z \geq 0.06$ SNe in the fit). Thus, if one assumes $\alpha = 2$, then SALT2 can be used to estimate t_{rise} with a typical uncertainty of $\sim$0.8 d. This scatter is only slightly worse than the median uncertainty on t_{rise}, $\sim$0.5 d, for individual SNe when adopting the $\alpha = 2$ prior (see §6). Furthermore, given that an $x_1 = 0$ SN is supposed to represent a "mean" SN Ia, Equation 3 suggests that the mean rise time of SNe Ia is $\sim$21 d.

If we repeat the same exercise using uninformative prior rise times for the volume limited sample, we find that the typical scatter about the linear t_{rise}-x_1 relation is $\sim$1.7 d and $\sim$1.4 d for the full and reliable subsets of this sample. The rise time of a mean SN according to this relation is $\sim$18 d, however, we caution that this scatter is likely too large and mean rise time too short, due to the systematic discussed in §5.2.

9.1.2. Precise Estimates of t_{rise} From Early Observations

While the t_{rise}–x_1 relation provides a relatively cheap method to infer the rise time of normal SNe Ia, a significant advantage of early observations is that they can provide far more precise estimates of t_{rise}, especially in the limit of high SNR. For the $\alpha = 2$ prior there are 14 SNe with a half 68% credible region that is < 3 hr. For the uninformative prior this number drops to two SNe. In either case, these measurements provide far more precision than possible from extrapolations based on SN Ia shape parameters (such as x_1).

While the methods adopted in this paper provide higher precision, it is impossible that they are both accurate. The median difference in the inferred t_{rise} from the $\alpha = 2$ and uninformative priors for individual SNe is 4.7 d. Even the volume-limited subset of SNe with reliable model parameters from the uninformative prior (15 total SNe) have a median difference of 2.8 d in t_{rise} for the two priors. The systematic effect identified in §5.2 suggests that the uninformative prior does not provide accurate estimates of t_{rise}, particularly for higher-z SNe. The $\alpha = 2$ prior, on the other hand, explicitly assumes that there is no change in the early optical colors of SNe Ia. Many SNe with early observations clearly invalidate this particular assumption, raising the possibility that neither method is accurate.

For t_{rise}, empirical evidence suggests that the uninformative prior underestimates the true rise time of SNe, meaning the $\alpha = 2$ prior may be more accurate (though again we caution that these estimates may also be inaccurate). A SN cannot be detected until it has exploded, and thus the epoch of discovery provides a lower limit on t_{rise}. Between PTF/iPTF (Papadogiannakis et al. 2019) and ZTF (Yao et al. 2019), there are $\sim$20 SNe Ia that are detected at least 18 d before $t_{B,\mathrm{max}}$, with a few detec-

tions as early as 21 d before $t_{B,\mathrm{max}}$. If the uninformative prior is accurate, then each of these SNe would represent an incredibly lucky set of circumstances: (i) they each have longer rise times than average ($\sim$18 d; see §7), and (ii) they were all discovered more or less immediately after t_{fl}. A more probable explanation is that the mean rise time is > 18 d, in which case the $\alpha = 2$ prior may provide a more accurate inference of the rise time. The fact that each of the 4 SNe with $z < 0.03$, which should have the least biased rise time estimates (see §5.2), have $t_{\mathrm{rise}} > 18$ d, further supports this claim.

9.1.3. Comparison to the Literature

Several studies in the literature have attempted to measure the mean rise time of SNe Ia. Here we compare our work to previous results. This exercise is somewhat fraught with difficulty, in the sense that each study incorporates slight differences in implementation, which, in turn, makes comparisons challenging. Furthermore, these studies are typically conducted with different filter sets and over a wide range of redshifts, which may introduce biases that are difficult to quantify across studies (as discussed above K-corrections are highly uncertain at very early epochs). Finally, the quality of the data in each of these studies is vastly different. For example, in Riess et al. (1999) there are only 6 SNe (and 10 total B-band observations) observed at phases ≤ -15 d, while our study includes 31 SNe discovered > 15 d before $t_{B,\mathrm{max}}$ (Yao et al. 2019). As we proceed with our cross-study comparison, we exclude rise time estimates for individual SNe and instead focus on studies with relatively large samples ($\gtrsim 10$ normal SNe Ia).

As previously outlined, there are broadly two different methods to measure the mean rise time of SNe Ia. The first uses the well established luminosity-decline relation for SNe Ia (Phillips 1993) to "shape correct" the SN light curves prior to fitting for the rise time. Thus, individual light curves are stretched by some empirically measured factor, and the mean rise time represents a normal SN Ia after shape correction (e.g., Riess et al. 1999; Aldering et al. 2000; Conley et al. 2006; Hayden et al. 2010; Ganeshalingam et al. 2011). The second method measures the rise time of each SN Ia within a sample, and then takes the mean of this distribution. These two methods are not equivalent, and therefore are likely to produce different results. If, for instance, a flux-limited survey finds more high-luminosity, slower-declining SNe than low-luminosity, faster-declining events, then the population mean will produce longer rise times than the shape-corrected mean.

Using different data sets obtained in very different redshift regimes, Riess et al. (1999), Aldering et al. (2000),

and Conley et al. (2006) estimate consistent values of the shape-corrected mean $t_{\rm rise} \approx 19.5$ d. Each of these studies fixes $\alpha = 2$ when fitting for the rise time. This estimate is roughly half way in between our estimates of the mean rise time from the uninformative prior and the $\alpha = 2$ prior. Later studies by Hayden et al. (2010) and Ganeshalingam et al. (2011), also provide estimates of the mean shape-corrected rise time and find smaller values of $\sim$17.5–18.0 d. As noted by Hayden et al., these methods are highly dependent on the template light curve used to stretch the individual SNe, and differences in the templates used by these studies may explain the dissensus between their findings.

The approach employed in Zheng et al. (2017), Papadogiannakis et al. (2019), and Firth et al. (2015) is more similar to the one adopted here, as each of these studies estimates the rise time for many individual SNe and then calculates the population mean. If the samples differ between any of these studies, and aside from 11 SNe that are included in both Papadogiannakis et al. (2019) and Firth et al. (2015) there is no overlap between any of those studies or this one, then it should be expected that the population mean rise time estimates will differ. Furthermore, the $t_{\rm rise}$ estimates in Papadogiannakis et al. (2019) and Firth et al. (2015) are not relative to $t_{B,\rm max}$, and it is known that the rise time increases as one progressively moves to redder wavelengths (e.g., Ganeshalingam et al. 2011). Taken together, this confluence of factors makes it difficult to compare results between these studies, which we nevertheless do below.

In Zheng & Filippenko (2017), a semi-analytical, six parameter, broken power-law model is introduced to describe the optical evolution of SNe Ia. This model has a distinct advantage over the methods employed here in that an artificial cutoff does not need to be applied in flux-space (see §3), though a post-peak cut must be applied as the model cannot reproduce the evolution of SNe into the nebular phase. A downside of this approach is that there are large degeneracies between the different model parameters, meaning it is difficult to find numerically stable solutions without fixing individual parameters to a single value (Zheng et al. 2017). For a sample of 56 well-observed low-z SNe this method produces a mean rise time of 16.0 d (Zheng et al. 2017), while the same technique applied to SNe Ia from PTF/iPTF finds a mean rise time of 16.8 d (Papadogiannakis et al. 2019). These estimates are considerably lower than the ones presented here, and are almost certainly underestimates of the true mean rise time based on the large number of SNe with detections >16 d before peak (Papadogiannakis et al. 2019; Yao et al. 2019). Indeed, close inspection of Figure 1 in Zheng et al. (2017) shows that

the six-parameter model underestimates the flux at the very earliest epochs and underestimates $t_{\rm rise}$ as a result.

The closest comparison to the methods used in this study can be drawn from Firth et al. (2015). Using a sample of 18 SNe discovered by PTF and the La Silla Quest (LSQ) survey, Firth et al. fit a model similar to Equation 1, in that $t_{\rm fl}$ and α are allowed to simultaneously vary. From these fits, they estimate a mean population $t_{\rm rise} = 18.98 \pm 0.54$ d, which is consistent with our estimate of the rise time for the volume-complete $z_{\rm host}$ sample, $\sim$18.5 d. Contrary to this study, they find shorter rise times, and a mean of $\sim$17.9 d, when fixing $\alpha = 2$ (this is likely explained by their adopted fit procedure, see §9.2).

9.2. The Expanding Fireball Model

The expanding fireball model (see §3) is remarkable in its simplicity. The two underlying assumptions of the expanding fireball model, that the photospheric velocity and temperature of the ejecta are $\sim$constant during the early evolution of the SN, are clearly over-simplifications (Parrent et al. 2012 shows that the photospheric velocity declines by at least 33% in the $\sim$5 d after explosion). Despite these simplifications, numerous studies have found that α is consistent with 2 (e.g., Conley et al. 2006; Hayden et al. 2010; Ganeshalingam et al. 2011; González-Gaitán et al. 2012; Zheng et al. 2017).

Based on the volume-limited subset of normal SNe Ia with reliable model parameters, we find a population mean $\alpha_r = 2.01 \pm 0.03$, which is consistent with the expanding fireball simplification. For α_g, on the other hand, we find a population mean of 2.13 ± 0.03, which is only marginally consistent with 2. As outlined above, it stands to reason that α would not equal 2 in every optical filter, as this would suggest SNe do not change colors shortly after explosion.

Furthermore, there are individual normal SNe Ia for which the expanding fireball model does not apply. This has been clearly shown for SN 2013dy, iPTF 16abc, and SN 2018oh (Zheng et al. 2013; Miller et al. 2018; Shappee et al. 2019; Dimitriadis et al. 2019), and within this study that is clearly the case for several of the lowest redshift SNe, with hence the highest SNR detections, in our sample:

- ZTF18aasdted (SN 2018big; $z \approx 0.018$, $\alpha_r \approx 1.4$),

- ZTF18abauprj (SN 2018cnw; $z \approx 0.024$, $\alpha_r \approx 2.2$),

- ZTF18abcflnz (SN 2018cuw; $z \approx 0.027$, $\alpha_r \approx 2.4$),

- ZTF18abfhryc (SN 2018dhw; $z \approx 0.032$, $\alpha_r \approx 3.3$),

- ZTF18abuqugw (SN 2018geo; $z \approx 0.031$, $\alpha_r \approx 2.7$).

In each of these cases the DIC clearly prefers $\alpha \neq 2$.

Given that many of the very best-observed, low-redshift SNe are incompatible with $alpha = 2$, and that the mean $alpha_g > 2$ in the ZTF sample, it stands to reason that the expanding fireball model does not adequately reproduce the observed diversity of SNe Ia at early phases. Nevertheless, according to the DIC, $\alpha = 2$ provides a reasonable proxy for the early evolution of the majority of normal SNe Ia (at the quality of ZTF high-cadence observations). This is either telling us that individual SNe exhibiting significant departures from $\alpha = 2$ are atypical (an interpretation adopted in Hosseinzadeh et al. 2017; Miller et al. 2018; Dimitriadis et al. 2019 and elsewhere), or, that for the vast majority of SNe the observations are not of a high enough quality to conclusively show $\alpha \neq 2$. Distinguishing between these two possibilities requires larger volume-limited samples.

Moving forward, it may be that the most appropriate prior for fitting the early evolution of SNe Ia is to adopt a Gaussian centered at 2 for α in the redder filters, while also placing a prior on the difference in α across different filters (for ZTF $\alpha_r - \alpha_g \approx -0.18$ based on §4.3). More observations, especially of low-z SNe, and testing, are needed to confirm whether or not such priors are in fact appropriate.

Finally, we note that the analysis in Firth et al. (2015) finds a mean value of $\alpha = 2.44 \pm 0.13$, which is not consistent with 2. This result can be understood in the context of the Firth et al. (2015) fitting procedure, whereby an initial estimate of t_{fl} is made by fixing $\alpha = 2$. Only observations obtained 2 days before and after this initial t_{fl} estimate are included in the final model fit (i.e., the entire baseline of non-detections is not used, as is done in this study). Truncating the baseline biases the model to longer rise times (as is observed in Firth et al. 2015), and, as shown in Figures 1, 2, and 3, longer rise times require larger values of α when adopting the model used here and in Firth et al. (2015).

The reason it is critical to test the expanding fireball model is that robust measurements of α can distinguish between different explosions scenarios. For example, the delayed-detonation models presented in Blondin et al. (2013), which provide a good match to SNe Ia at maximum light, systematically over estimate the power-law index at early times (with typical values of $\alpha \approx 7$, see Figure 1 in Dessart et al. 2014). This led Dessart et al. (2014) to alternatively consider pulsational-delayed detonation models, which do result in a smaller power-law index ($\alpha \approx 3$), though those results are still incompati-

ble with what we find here.[10] In Noebauer et al. (2017), the early evolution of various explosion models does not follow an exact power-law. They find an almost power-law evolution for pure deflagration models, which may explain the origin of 02cx-like SNe. For the pure deflagrations Noebauer et al. (2017) find $\alpha < 2$, which qualitatively agrees with our results for ZTF18abclfee (SN 2018cxk), where $\alpha_r \approx 1$ (see §8). The models presented in Magee et al. (2019), which examine the evolution of SNe with different ^{56}Ni distributions, provide good qualitative agreement to what we find for ZTF SNe. Magee et al. (2019) find that the rising power-law index is larger in the B-band than the R-band (similar to what we see in g_{ZTF} and r_{ZTF}), and that the mean value of these distributions is ~ 2. As suggested in Magee et al. (2019), it may be the case that the vast majority of the differences observed in the early ZTF light curves can be explained via variations in the ^{56}Ni mixing in the SN ejecta.

10. Conclusions

In this paper we have presented an analysis of the initial evolution and rise times of 127 ZTF-discovered SNe Ia with early observations (see Yao et al. 2019 for details on how the sample was selected). These SNe were observed as part of the ZTF high-cadence extragalactic experiment, which obtained 3 g_{ZTF} and 3 r_{ZTF} observations every night the telescope was open. A key distinction of this data set relative to many previous studies is the large number of observations taken prior to the epoch of discovery, which meaningfully constrains the behavior of the SN at very early times (see C.2). The uniformity, size and observational duty cycle of this data set are truly unique, making this sample of ZTF SNe the premiere data set for studying the early evolution of thermonuclear SNe.

We model the early evolution of these SNe as a power-law in time t, whereby the flux $f \propto (t - t_{\mathrm{fl}})^{\alpha}$, where t_{fl} is the time of first light, and α is the power-law index. By simultaneously fitting observations in the g_{ZTF} and r_{ZTF} filters, we are able to place stronger constraints on t_{fl} than would be possible with observations in a single filter. While many previous studies have fixed $\alpha = 2$, following the simple expanding fireball model (e.g., Riess et al. 1999), we have instead allowed α to vary, as there are recent examples of SNe Ia where α clearly is not

---

[10] The range of α values reported in Dessart et al. (2014) is fit to the first ~ 3 d after explosion. Fitting all observations with $f_{\mathrm{obs}} \leq 0.4 f_{\mathrm{max}}$, as is done in this study, would reduce the inferred values of α in Dessart et al. (2014), possibly bringing them in line with those found in this study.

equal to 2 (e.g., Zheng et al. 2013; Miller et al. 2018; Shappee et al. 2019; Dimitriadis et al. 2019). While the population mean value of α tends towards 2, there are several individual SNe featuring an early evolution that deviates from an $\alpha = 2$ power-law, justifying our model parameterization.

As might be expected, we find that our ability to constrain the model parameters is highly dependent on the quality of the data. SNe Ia at low redshifts that lack significant gaps in observational coverage are better constrained than their high-redshift counterparts or events will large temporal gaps. We identify those SNe with reliable model parameters under the reasonable assumption that models of the initial flux evolution should over-estimate the flux at peak brightness. Following this procedure we find that 51 of the SNe have reliable model parameters. We focus our analysis on these events.

For the subset of normal SNe with reliable model parameters we estimate a population mean $t_{\rm rise} \approx 18.0\,{\rm d}$, with a sample standard deviation of $\sim 1.6\,{\rm d}$. For individual SNe, the range of rise times extends from ~ 14–$22\,{\rm d}$. We have additionally identified a systematic in the parameter estimation for models that simultaneously vary $t_{\rm fl}$ and α. Namely, for flux-limited surveys, the model constraints on $t_{\rm rise}$ will be systematically underestimated for the higher redshift SNe in the sample. If we restrict the sample to a volume-limited subset of SNe ($z < 0.06$), where this bias may still be present but probably less prevalent, we estimate a mean population rise time of $\sim 18.5\,{\rm d}$.

Normal SNe Ia have a population mean $\alpha_g \approx 2.1$ and a population mean $\alpha_r \approx 2.0$, with a population standard deviation ~ 0.5 for both parameters. While the mean value for our sample of SNe tends towards 2, as would be expected in the expanding fireball model, we observe a range in α extending from ~ 1.0–3.5. For both $t_{\rm rise}$ and α, there is no single value that is consistent with all the SNe in our sample. Interestingly, however, we do find that nearly all SNe are consistent with a single value of $\alpha_r - \alpha_g$, which describes the initial $g_{\rm ZTF} - r_{\rm ZTF}$ color evolution of SNe Ia. The data show a mean value of $\alpha_r - \alpha_g \approx -0.18$, meaning the optical colors of most SNe Ia evolve to the blue with comparable magnitudes over a similar timescale. This could be a sign that the degree of ^{56}Ni-mixing in the SN ejecta is very similar for the majority of SNe Ia (e.g., Piro & Morozova 2016; Magee et al. 2018, 2019).

We find that the rise time is correlated with the light curve shape of the SN, in the sense that high-luminosity, slowly-declining SNe have longer rise times. This finding is consistent with many previous studies.

Given the large number of SNe with unreliable model parameters, and the observed bias in the measurement of $t_{\rm rise}$ for high-z SNe, we also consider how the model parameter estimates change with strong priors. In particular, we adopt $\alpha_g = \alpha_r = 2$, enforcing the expanding fireball hypothesis on the data. Strictly speaking, this prior means that the early colors of SNe Ia do not change, which we empirically know is not the case. Nevertheless, a $\sim$constant temperature is one of the assumptions of the fireball model, and, thus we proceed.

Under the $\alpha = 2$ prior, we find that far more SNe have reliable $t_{\rm rise}$ estimates. For the typical SN in our sample, fixing $\alpha = 2$ results in an increase in $t_{\rm rise}$ by a few days. We estimate a population mean $t_{\rm rise} \approx 21.0\,{\rm d}$ when adopting the $\alpha = 2$ prior. One consequence of adopting this prior is that it significantly reduces the previously observed bias where high-z SNe are inferred to have shorter rise times. The use of this prior also reduces the scatter in the x_1–$t_{\rm rise}$ relation, and we find that with SALT2, via the measurement of x_1, it is possible to estimate $t_{\rm rise}$ with a typical scatter of $\sim 0.77\,{\rm d}$, even if there are no early time observations available. We also find that, for the vast majority of the SNe in our sample, all but 13 events, there is only weak evidence that the $\alpha \neq 2$ model is preferred to a model with $\alpha_g = \alpha_r = 2$ according to the DIC.

While we have primarily focused on the properties and evolution of normal SNe Ia, there are 7 SNe in our sample that cannot be categorized as normal (see Yao et al. 2019). As in previous studies, we find that the rise times of Ia-CSM SNe and SC explosions are longer than those of normal SNe Ia. We highlight our observations of ZTF18abclfee (SN 2018cxk), an 02cx-like SN with exquisite observational coverage in the time before explosion. We estimate the $t_{\rm fl}$ to within $\sim 8\,{\rm hr}$ for ZTF18abclfee, making our measurement the most precise estimate of $t_{\rm rise}$ for any 02cx-like SN to date. ZTF18abclfee took $\sim 10\,{\rm d}$ to reach peak brightness, roughly $5\,{\rm d}$ less than SN 2005hk, another 02cx-like event with a well-constrained rise time.

This study has important lessons for future efforts to characterize the rise times of SNe Ia. We have found that for all but the best-observed, highest SNR events, a generic power-law model where α is allowed to vary does not place meaningful constraints on the $t_{\rm rise}$, or worse, in the case of high-z events, it produces a biased estimate. If this were the end of the story, it would be particularly bad news for LSST, which will typically have several day gaps in its observational cadence (Ivezić et al. 2008). With only Equation 1 at our disposal, we would rarely be able to infer $t_{\rm rise}$ for LSST SNe. We have also shown, however, that in the

limit of low-quality data, the application of a prior to the model can significantly improve the final inference. Our current challenge is to develop an empirically motivated prior for the model parameters. This provides a strong justification for the concurrent operation of LSST and small-aperture, high-cadence experiments, such as ZTF and the planned ZTF-II. These smaller, more focused, missions can provide exquisite observations of a select handful of SNe that can be used to drive the priors in our inference. While there have been thousands of SNe Ia studied to date (e.g., Jones et al. 2017), indeed more examples are still needed: there are only 4 normal, $z < 0.03$ SNe Ia in our sample, and these 4 are nearly as valuable as the remainder of the sample for establishing the diversity of SNe Ia. As we improve our understanding of these priors, and combine that knowledge with the hitherto unimaginable statistical samples from LSST (∼millions of SNe), we will definitively understand the early evolution and rise time distribution of Type Ia SNe.

Appendix A   Updated Priors Following the Change of Variables

As mentioned in §3, there is a strong degeneracy in the posterior estimates of A and α. This degeneracy can be removed under the change of variables from (A, α) to (A', α'), where $A' = A10^{\alpha}$ and $\alpha' = \alpha$. From the Jacobian of this transformation, we find

$$P(A', \alpha') = 10^{-\alpha'} P(A, \alpha).$$

The change in variables should not affect the prior probability, therefore,

$$P(A', \alpha') = 10^{-\alpha'} P(A'10^{-\alpha'}, \alpha'), \qquad \text{(A1)}$$

which can be satisfied by:

$$P(A', \alpha') \propto A'^{-1} 10^{-\alpha'}. \qquad \text{(A2)}$$

While Equation A1 is also satisfied by $P(A', \alpha') \propto A'^{-1}$, adopting this as the joint prior on (A', α') does not remove the degeneracy between the parameters as A' absorbs the multiplicative factor of 10^{α}, effectively reducing the problem to be the same as it was before the change of variables. Thus, as listed in Table 1, we adopt Equation A2 as the prior on the transformed variables, which we find breaks the degeneracy (see Figures 1, 2, and 3).

Appendix B   Quality Assurance

As noted in §3, the MCMC model converges for all but one ZTF SNe within the sample. However, visual inspection of both the corner plots and individual draws from the posterior quickly reveals that for some SNe the
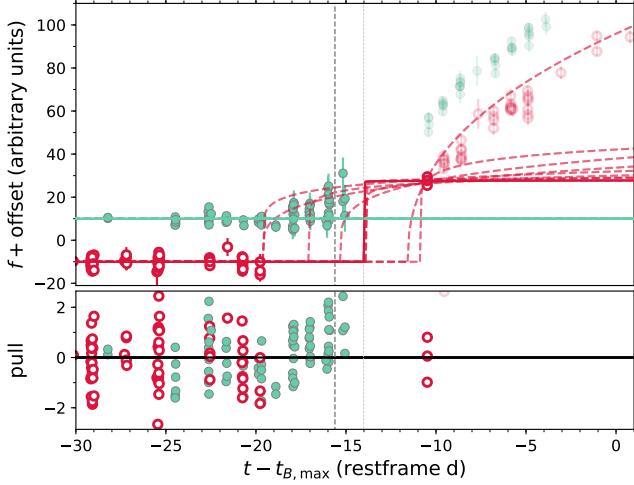
Figure B1. Same as the bottom panel of Figure 1 for ZTF18aaqffyp (SN 2018bhr), a SN with observations that place very weak constraints on t_{fl}. The marginalized posteriors for A' and α are essentially identical to the priors. Posteriors with little information beyond the prior are typical of SNe with significant observational gaps.

data do not provide strong constraints on the model parameters (see Figure 3). In the most extreme cases, as shown in Figure B1, large gaps in the observations make it nearly impossible to constrain the model parameters. For these cases, the model posteriors are essentially identical to the priors (there is always a weak constraint on t_{fl} from epochs where the SN is not detected).

To identify SNe with poor observational coverage, or unusual structure in the posterior, we visually examine the light curves and corner plots for each of the 127 SNe in our sample. We flag SNe where the model significantly underestimates the flux near $t_{B,\mathrm{max}}$ (similar to what is shown in Figure B1), as this is a good indicator that the model has poor predictive value. By definition the light curve derivative is zero at maximum light, and the relative change in brightness constantly slows down in the ∼week leading up to maximum light. Therefore, models of the early emission should greatly over-predict the flux at maximum, which is why we adopt this criterion for flagging SNe with poorly constrained model parameters.

Numerically, the visually flagged SNe can, for the most part, be identified by a combination of two criteria: the 90% credible region on t_{fl}, CR_{90}, and the number of nights on which the SN was detected. Rather than providing a threshold for detection (e.g., 3σ, 5σ, etc.), we count all nights with $f_{\mathrm{mean}} \leq 0.4 f_{\mathrm{max}}$ after the median marginalized posterior value of t_{fl} with observations in either the g_{ZTF}, r_{ZTF}, or both filters, $N_{g,\mathrm{det}}$, $N_{r,\mathrm{det}}$, and $N_{gr,\mathrm{det}}$, respectively. We take the geometric mean of
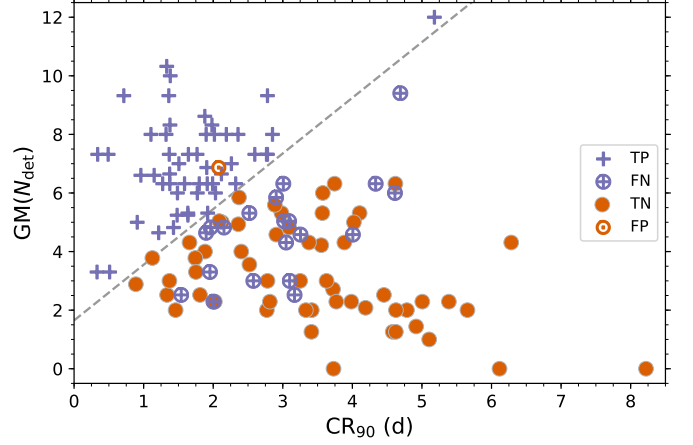
Figure B2. Scatter plot showing the distribution of the 127 ZTF SNe Ia in the $\mathrm{GM}(N_{\mathrm{det}})$–$\mathrm{CR}_{90}$ plane. Models with flagged posterior parameters are shown as orange circles, while those that are not flagged are shown via + symbols. The dashed line shows the adopted separation threshold for identifying reliable model fits (above the line), and unreliable model fits. FP and FN (see text) SNe are circled.

these three numbers to derive the "average" number of nights on which the SN was detected, $\mathrm{GM}(N_{\mathrm{det}})$. A scatter plot showing $\mathrm{GM}(N_{\mathrm{det}})$ vs. CR_{90} is shown in Figure B2. Visually flagged SNe are shown as orange circles, while + symbols show those that were not flagged.

The visual inspection procedure described above is not fully reproducible (visual inspection is by its very nature subjective). Therefore, we aim to separate the SNe into two classes (reliable and unreliable) via an automated, systematic procedure. Treating the visually flagged sources as the negative class, we view false positives (i.e., visually flagged SNe that are included in the final population analysis) particularly harmful. Therefore, we adopt

$$\mathrm{GM}(N_{\mathrm{det}}) \geq 1.9\,\mathrm{CR}_{90} + 1.65,$$

as the classification threshold for reliable model fits (as shown via the dashed line in Figure B2). This threshold retains 50 true positives (TP; visually good models included in the final sample) with only a single false positive (FP; visually flagged SNe in the final sample). This choice does result in 20 false negatives (FN; visually good models *excluded* from the final sample), while all remaining flagged SNe are true negatives (TN). Further scrutiny of the FN reveals several light curves with significant observational gaps, which, as discussed above, makes it difficult to place strong constraints on the model parameters. Ultimately, our two-step procedure identifies 51 SNe as reliable, while 76 are excluded from the final population analysis due to their unreliable constraints on the model parameters.

Appendix C Systematics

C.1 Definition of "Early" for Model Fitting

In §3 we highlighted that there is no single agreed upon definition of which SN Ia observations are best for modeling the early evolution of SNe Ia. Throughout this study we have adopted a threshold, f_{thresh}, relative to the maximum observed flux, $f_{\max}$, whereby we define all observations less than $f_{\mathrm{thresh}} = 0.4$ the maximum in each filter ($f_{\mathrm{obs}} \leq 0.4 f_{\max}$) as the early portion of the light curve. As noted in §3, setting $f_{\mathrm{thresh}} = 0.4$, is arbitrary (although consistent with some previous studies). Here we examine the effect of this particular choice if we had instead adopted $f_{\mathrm{thresh}} = 0.25, 0.30, 0.35, 0.45$, or 0.50 for the fitting procedure in §3.

There are 12 SNe for which the MCMC chains did not converge for one or more of the alternative flux thresholds. They are excluded from the analysis below. For the remaining 115 SNe in our sample, we consider the model parameters to be consistent if the marginalized, 1-dimensional 90% credible regions for the three parameters that we care about, t_{fl}, α_g, and α_r, overlap with the estimates when $f_{\mathrm{thresh}} = 0.40$.[11] This definition identifies substantial differences in the final model parameters while varying f_{thresh} over a reasonable range. Of the 115 SNe with converged chains, we find that 98 ($> 85\%$ of the sample) have marginalized, 1-D posterior credible regions consistent with the results for $f_{\mathrm{thresh}} = 0.40$, independent of the adopted value of f_{thresh}. 15 of the 17 SNe that do not have consistent t_{fl}, α_g, or α_r estimates feature gaps in observational coverage, which is the likely reason for the inconsistency. As f_{thresh} increases from 0.25–0.5, the information content dramatically changes before and after a gap leading to significantly different parameter estimates.

If we alternatively consider the results to be consistent only if the 68% credible regions agree with the $f_{\mathrm{thresh}} = 0.40$ results, then only 64 SNe have consistent parameters as f_{thresh} varies. This suggests that while the results are largely consistent, the central mass of the posterior density is affected by which data are, and are not, included in the model fit. In Figure C3, we show how the estimates of t_{fl} and α_g change as a function of f_{thresh} for SNe with consistent model parameters. Note that, by construction, the 90% credible regions for each SN overlap at every value of f_{thresh}, and thus, for clarity, we omit error bars.

To identify trends with f_{thresh}, we define SNe with both $\alpha_g(f_{\mathrm{thresh}} = 0.5)$ and $\alpha_g(f_{\mathrm{thresh}} = 0.45)$ greater
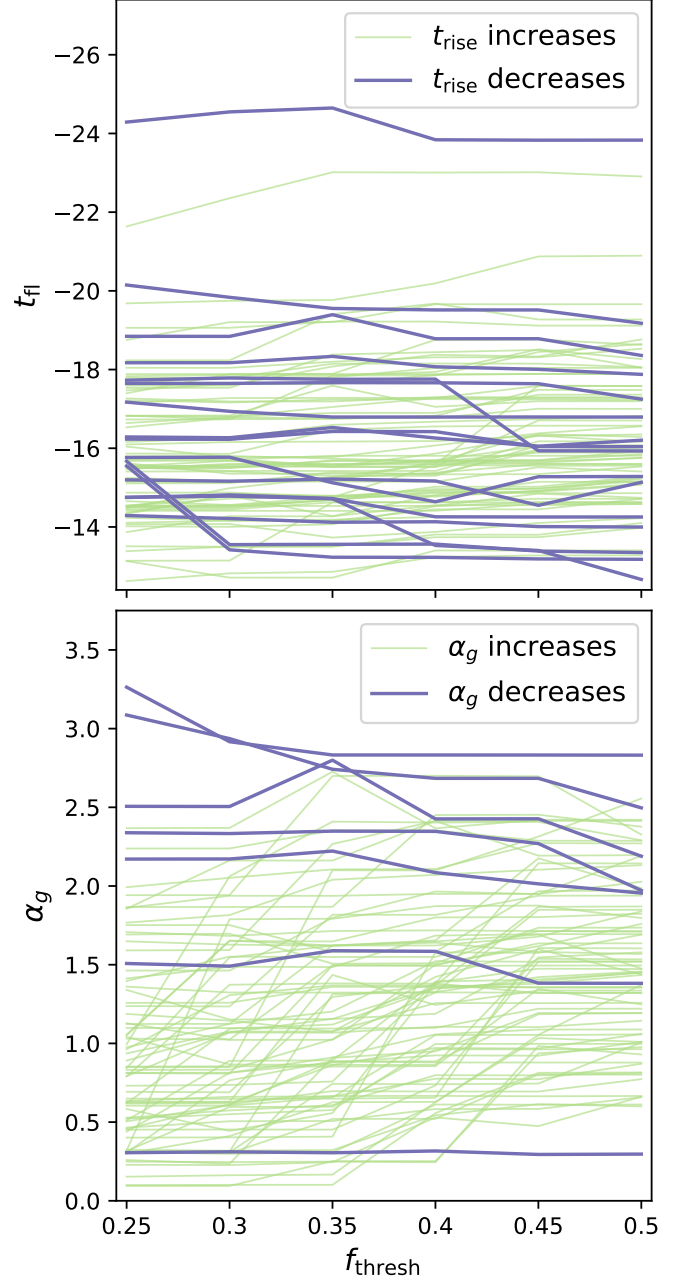
Figure C3. Evolution of the inferred values of t_{fl} and α_g as f_{thresh} is increased from 0.25 to 0.5. Only SNe with consistent model parameters, that nevertheless show evidence for increasing or decreasing with f_{thresh}, are shown (see text for a definition of consistent, increasing, and decreasing). Thin green lines show SNe where t_{rise} or α_g increases as more observations are included in the model, while thick purple lines show SNe for which these values decline. We find that for the vast majority of SNe, as additional observations are included in the model fit, both t_{rise} and α_g increase.

than both $\alpha_g(f_{\mathrm{thresh}} = 0.25)$ and $\alpha_g(f_{\mathrm{thresh}} = 0.3)$ to show evidence for α_g increasing with f_{thresh}. We define

---

[11] Given the strong correlation between α_g and α_r (see §5.1), we discuss only α_g below.

α_g as decreasing in cases where the opposite is true. 75 of the 98 SNe with consistent model parameters show evidence for α_g increasing with f_{thresh}, while only 7 show evidence for a decline. Using a similar definition for t_{rise} (note that decreasing t_{fl} corresponds to increasing t_{rise}), we find that in 68 SNe t_{rise} increases with f_{thresh}, while in 16 SNe t_{rise} decreases as more observations are included in the fit. Thus, the vast majority of SNe exhibit an increase in α_g and t_{fl} as f_{thresh} is increased. Figure C3 shows that the magnitude of this trend is much larger for α_g than t_{rise}, which makes sense. When there are few SN detections, which is more likely when f_{thresh} is low, small values of α fit the data well, as in Figure B1. Including more information about the rise, by increasing f_{thresh}, results in very-low values of α no longer being consistent with the data. t_{fl}, on the other hand, is strongly constrained by the first epoch of detection (see §5.2). In this case the addition of more observations will not lead to as dramatic an effect.

C.2 The Importance of Pre-Explosion Observations

A unique, and important, component of our ZTF data set is the nightly collection of multiple observations. Yao et al. (2019) demonstrated that such an observational sequence enables low-SNR detections of the SN prior to the traditional 5σ discovery epoch (see Masci et al. 2019), which can provide critical constraints on t_{fl}. Many previous studies utilize filtered observations that are obtained $\sim$1 d, or more, after the epoch of discovery (e.g., Riess et al. 1999; Aldering et al. 2000; Gane-shalingam et al. 2010; Zheng et al. 2017). To demonstrate the importance of the ZTF sub-threshold detections, we re-fit the model from §3 to each of our ZTF light curves *after removing all observations before and on the night the SN is first detected* (i.e., SNR $\geq$ 5, as defined in Yao et al. 2019).

Following the removal of these observations, the MCMC chains converge (see §3) for only 10 SNe. This is understandable as the removal of the "baseline" observations makes it very difficult to constrain C_d and β_d. The removal of these observations leads to dramatically different estimates of the model parameters for these 10 SNe. Thus, we report the results given the strong trends, though we caution that these results are somewhat preliminary and should be confirmed with more detailed simulations.

With the baseline observations removed, the inferred value of t_{fl} increases (i.e., t_{rise} decreases) for all 10 SNe relative to the results from §3. The median difference of this shift is $\sim$3.5 d. Using the definition of agreement from C.1, i.e., overlap in the 90% credible regions, only 3 of the 10 SNe have estimates of t_{fl} that agree after removing the non-detections. Removing the baseline observations also decreases estimates of α (which agrees with the trend seen in Figure 7), with only 5 of the 10 SNe having estimates of α_g and α_r that agree. These trends suggest that pre-explosion observations are critically needed to produce accurate estimates of t_{rise} (though, again, we caution that these results should be confirmed with a larger sample of SNe).

References

Aldering, G., Knop, R., & Nugent, P. 2000, AJ, 119, 2110

Aldering, G., Antilogus, P., Bailey, S., et al. 2006, ApJ, 650, 510

Amanullah, R., Lidman, C., Rubin, D., et al. 2010, ApJ, 716, 712

Arnett, W. D. 1982, ApJ, 253, 785

Astropy Collaboration, Robitaille, T. P., Tollerud, E. J., et al. 2013, A&A, 558, A33

Barbary, K., Barclay, T., Biswas, R., et al. 2016, SNCosmo: Python library for supernova cosmology

Bellm, E. C., Kulkarni, S. R., Graham, M. J., et al. 2019a, Publications of the Astronomical Society of the Pacific, 131, 018002

Bellm, E. C., Kulkarni, S. R., Barlow, T., et al. 2019b, PASP, 131, 068003

Bianco, F. B., Howell, D. A., Sullivan, M., et al. 2011, ApJ, 741, 20

Blondin, S., Dessart, L., Hillier, D. J., & Khokhlov, A. M. 2013, MNRAS, 429, 2127

Bloom, J. S., Kasen, D., Shen, K. J., et al. 2012, ApJL, 744, L17

Cao, Y., Kulkarni, S. R., Howell, D. A., et al. 2015, Nature, 521, 328

Conley, A., Howell, D. A., Howes, A., et al. 2006, AJ, 132, 1707

De, K., Kasliwal, M. M., Polin, A., et al. 2019, ApJL, 873, L18

Dessart, L., Blondin, S., Hillier, D. J., & Khokhlov, A. 2014, MNRAS, 441, 532

Dilday, B., Howell, D. A., Cenko, S. B., et al. 2012, Science, 337, 942

Dimitriadis, G., Foley, R. J., Rest, A., et al. 2019, ApJL, 870, L1

Fausnaugh, M. M., Vallely, P. J., Kochanek, C. S., et al. 2019, arXiv, arXiv:1904.02171

Firth, R. E., Sullivan, M., Gal-Yam, A., et al. 2015, MNRAS, 446, 3895

Foreman-Mackey, D. 2016, JOSS, 24

Foreman-Mackey, D., Hogg, D. W., Lang, D., & Goodman, J. 2013, PASP, 125, 306

Ganeshalingam, M., Li, W., & Filippenko, A. V. 2011, MNRAS, 416, 2607

Ganeshalingam, M., Li, W., Filippenko, A. V., et al. 2010, ApJS, 190, 418

González-Gaitán, S., Conley, A., Bianco, F. B., et al. 2012, ApJ, 745, 44

Goodman, J., & Weare, J. 2010, CAMCS, 5, 65

Graham, M. J., Kulkarni, S. R., Bellm, E. C., et al. 2019, PASP, 131, 078001

Guy, J., Astier, P., Baumont, S., et al. 2007, A&A, 466, 11

Hayden, B., Rubin, D., & Strovink, M. 2019, ApJ, 871, 219

Hayden, B. T., Garnavich, P. M., Kessler, R., et al. 2010, ApJ, 712, 350

Hogg, D. W., Bovy, J., & Lang, D. 2010, ArXiv e-prints

Hosseinzadeh, G., Sand, D. J., Valenti, S., et al. 2017, ApJL, 845, L11

Howell, S. B., Sobeck, C., Haas, M., et al. 2014, PASP, 126, 398

Hunter, J. D. 2007, Computing In Science & Engineering, 9, 90

Ivezić, Ž., Tyson, J. A., Acosta, E., et al. 2008, ArXiv e-prints

Jeffreys, H. 1946, Proceedings of the Royal Society of London. Series A. Mathematical and Physical Sciences, 186, 453

—. 1961, Theory of probability, Third edition (Clarendon Press, Oxford), ix+447

Jiang, J.-A., Doi, M., Maeda, K., et al. 2017, Nature, 550, 80

Jones, D. O., Scolnic, D. M., Riess, A. G., et al. 2017, ApJ, 843, 6

Jones, D. O., Scolnic, D. M., Foley, R. J., et al. 2019, ApJ, 881, 19

Jones, E., Oliphant, T., Peterson, P., et al. 2001–, SciPy: Open source scientific tools for Python

Kasen, D. 2010, ApJ, 708, 1025

Kasliwal, M. M., Cannella, C., Bagdasaryan, A., et al. 2019, PASP, 131, 038003

Kromer, M., Fremling, C., Pakmor, R., et al. 2016, MNRAS, 459, 4428

Law, N. M., Kulkarni, S. R., Dekany, R. G., et al. 2009, PASP, 121, 1395

Livio, M., & Mazzali, P. 2018, PhR, 736, 1

Magee, M. R., Maguire, K., Kotak, R., et al. 2019, arXiv, arXiv:1912.07603

Magee, M. R., Sim, S. A., Kotak, R., & Kerzendorf, W. E. 2018, A&A, 614, A115

Maoz, D., Mannucci, F., & Nelemans, G. 2014, ARA&A, 52, 107

Marion, G. H., Brown, P. J., Vinkó, J., et al. 2016, ApJ, 820, 92

Masci, F. J., Laher, R. R., Rusholme, B., et al. 2019, PASP, 131, 018003

McKinney, W. 2010, 51

Miller, A. A., Kasliwal, M. M., Cao, Y., et al. 2017, ApJ, 848, 59

Miller, A. A., Cao, Y., Piro, A. L., et al. 2018, ApJ, 852, 100

Noebauer, U. M., Kromer, M., Taubenberger, S., et al. 2017, MNRAS, 472, 2787

Nomoto, K. 1982a, ApJ, 253, 798

—. 1982b, ApJ, 257, 780

Nugent, P. E., Sullivan, M., Cenko, S. B., et al. 2011, Nature, 480, 344

Olling, R. P., Mushotzky, R., Shaya, E. J., et al. 2015, Nature, 521, 332

Papadogiannakis, S., Goobar, A., Amanullah, R., et al. 2019, MNRAS, 483, 5045

Parrent, J. T., Howell, D. A., Friesen, B., et al. 2012, ApJL, 752, L26

Pedregosa, F., Varoquaux, G., Gramfort, A., et al. 2011, Journal of Machine Learning Research, 12, 2825

Perlmutter, S., Aldering, G., Goldhaber, G., et al. 1999, ApJ, 517, 565

Phillips, M. M. 1993, ApJL, 413, L105

Phillips, M. M., Li, W., Frieman, J. A., et al. 2007, PASP, 119, 360

Piro, A. L., & Morozova, V. S. 2016, ApJ, 826, 96

Piro, A. L., & Nakar, E. 2013, ApJ, 769, 67

—. 2014, ApJ, 784, 85

Polin, A., Nugent, P., & Kasen, D. 2019, ApJ, 873, 84

Prieto, J. L., Garnavich, P. M., Phillips, M. M., et al. 2007, ArXiv e-prints, 706

Rau, A., Kulkarni, S. R., Law, N. M., et al. 2009, PASP, 121, 1334

Ricker, G. R., Winn, J. N., Vanderspek, R., et al. 2015, JATIS, 1, 014003

Riess, A. G., Filippenko, A. V., Challis, P., et al. 1998, AJ, 116, 1009

Riess, A. G., Filippenko, A. V., Li, W., et al. 1999, AJ, 118, 2675

Riess, A. G., Macri, L. M., Hoffmann, S. L., et al. 2016, ApJ, 826, 56

Scalzo, R. A., Ruiter, A. J., & Sim, S. A. 2014, MNRAS, 445, 2535

Scalzo, R. A., Aldering, G., Antilogus, P., et al. 2010, ApJ, 713, 1073

Scolnic, D. M., Jones, D. O., Rest, A., et al. 2018, ApJ, 859, 101

Shappee, B. J., Piro, A. L., Stanek, K. Z., et al. 2016a, ArXiv e-prints

Shappee, B. J., Piro, A. L., Holoien, T. W.-S., et al. 2016b, ApJ, 826, 144

Shappee, B. J., Holoien, T. W. S., Drout, M. R., et al. 2019, ApJ, 870, 13

Shen, K. J., Boubert, D., Gänsicke, B. T., et al. 2018, ApJ, 865, 15

Silverman, J. M., Ganeshalingam, M., Li, W., et al. 2011, MNRAS, 410, 585

Silverman, J. M., Nugent, P. E., Gal-Yam, A., et al. 2013, ApJS, 207, 3

Spiegelhalter, D. J., Best, N. G., Carlin, B. P., & Van
    Der Linde, A. 2002, Journal of the royal statistical
    society: Series b (statistical methodology), 64, 583
Webbink, R. F. 1984, ApJ, 277, 355
Whelan, J., & Iben, Icko, J. 1973, ApJ, 186, 1007
Yao, Y., Miller, A. A., Kulkarni, S. R., et al. 2019, ApJ,
    886, 152

Zackay, B., Ofek, E. O., & Gal-Yam, A. 2016, ApJ, 830, 27
Zheng, W., & Filippenko, A. V. 2017, ApJL, 838, L4
Zheng, W., Kelly, P. L., & Filippenko, A. V. 2017, ApJ,
    848, 66
Zheng, W., Silverman, J. M., Filippenko, A. V., et al. 2013,
    ApJL, 778, L15
Zheng, W., Shivvers, I., Filippenko, A. V., et al. 2014,
    ApJL, 783, L24